Theory of local electric polarization and its relation to internal strain: Impact on polarization potential and electronic properties of group-III nitrides

Miguel A. Caro,[1,2,*] Stefan Schulz,[1] and Eoin P. O'Reilly[1,2]
[1]*Photonics Theory Group, Tyndall National Institute, Dyke Parade, Cork, Ireland*
[2]*Department of Physics, University College Cork, Cork, Ireland*
(Received 11 September 2013; revised manuscript received 21 October 2013; published 3 December 2013)

We present a theory of local electric polarization in crystalline solids and apply it to study the case of wurtzite group-III nitrides. We show that a local value of the electric polarization, evaluated at the atomic sites, can be cast in terms of a summation over nearest-neighbor distances and Born effective charges. Within this model, the local polarization shows a direct relation to internal strain and can be expressed in terms of internal strain parameters. The predictions of the present theory show excellent agreement with a formal Berry-phase calculation for random distortions of a test-case CuPt-like InGaN alloy and InGaN supercells with randomly placed cations. While the present level of theory is appropriate for highly ionic compounds, such as III-N materials, we show that a more complex model is needed for less ionic materials, such as GaAs, in which the strain dependence of Born effective charges has to be taken into account. Moreover, we provide *ab initio* parameters for GaN, InN, and AlN, including hybrid functional values for the piezoelectric coefficients and the spontaneous polarization, which we use to accurately implement the local theory expressions. In order to calculate the local polarization potential, we also present a point dipole method. This method overcomes several limitations related to discretization and resolution which arise when obtaining the local potential by solving Poisson's equation on an atomic grid. Finally, we perform tight-binding supercell calculations to assess the impact of the local polarization potential arising from alloy fluctuations on the electronic properties of InGaN alloys. In particular, we find that the large upward bowing with composition of the InGaN valence-band edge is strongly influenced by local polarization effects. Furthermore, our analysis allows us to extract composition-dependent bowing parameters for the energy gap and valence- and conduction-band edges.

DOI: 10.1103/PhysRevB.88.214103 PACS number(s): 77.65.−j, 31.15.aq, 71.20.Mq

I. INTRODUCTION

Electrostatic built-in fields arising from discontinuities of the electric polarization vector significantly modify the electronic and optical properties of semiconductor nanostructures.[1–4] Of particular interest are systems such as GaAs-based quantum dots (QDs), whose electronic and optical properties are affected by the symmetry of strain and strain-induced piezoelectric fields.[5,6] The effect of built-in electrostatic fields is even more dramatic in III-N-based heterostructures, where the large piezoelectric response together with the intrinsic spontaneous polarization give rise to built-in electrostatic fields far exceeding those encountered for other III-V materials.[1,7–12] Although these effects have been studied over the last two decades, the possible role of the *local* polarization potential has only recently been considered.[4]

Theoretical studies that include a treatment of polarization fields effectively treat the field at a continuum level (even if the strain itself is obtained from an atomistic calculation), with the polarization assumed to have a smooth behavior with local strain and composition, even in the case of alloys. We have previously shown for InGaN alloys that a local value of polarization can be obtained, observing large fluctuations in its value at a microscopic scale.[4] In this paper we lay our theory of local polarization on more solid ground, giving general equations and providing a direct link with internal strain. We provide a complete and consistent set of polarization-related *ab initio* parameters for the group-III nitrides, which are needed for the computation of the local and macroscopic contributions to the total polarization. In order to compute the electric potential arising from the local polarization, we also present a "point dipole" method.

When computing the electronic properties of alloyed materials, it is of vital importance that the supercell used allows to reproduce the different configurations encountered in actual material samples. In practice, this implies that the supercell must be sufficiently large. At present, calculations for such large systems escape the reach of *ab initio* techniques, such as density functional theory (DFT). Moreover, standard implementations of DFT fail to correctly describe band gaps,[13] and those implementations that allow an accurate prediction of this quantity, such as hybrid approaches,[14] are computationally much more expensive. On the other hand, alternative semiempirical electronic structure methods enable access to the electronic properties of large systems for which first-principles approaches cannot be realistically implemented. The tight-binding approximation allows an accurate description of the electronic structure in these cases, with the advantage that polarization potentials and deformation potentials can be included as on-site corrections to the Hamiltonian matrix elements.[15,16] We therefore apply the tight-binding scheme in this work in order to get insight into how the strong local polarization effects influence the electronic structure of InGaN alloys.

The paper is organized as follows. In Sec. II, we introduce the theoretical foundations of the present theory of local electric polarization and discuss its degree of validity. In particular, we show in Sec. II C by comparing our local polarization results to DFT calculations that the first-order level of description presented here works remarkably well in

the case of group-III nitrides (relevant *ab initio* parameters for GaN, AlN, and InN are given in Sec. II C 1). In Sec. III, we present a point dipole method for the computation of the local polarization potential on an atomic grid, and discuss practical considerations regarding the implementation of the method. Practical examples of the calculation of local polarization and local polarization potential are given in Sec. IV for polar and non polar InGaN/GaN quantum wells (QWs). In Sec. V, we present a tight-binding (TB) model for the calculation of the electronic structure in nitride systems, and discuss how the local polarization potential affects the band gap of InGaN. We then extract composition-dependent bowing parameters for the band gap and for both the conduction band (CB) and valence-band (VB) edges of InGaN alloys over the whole composition range in Sec. VI. Finally, we summarize our conclusions in Sec. VII.

II. THEORY OF LOCAL ELECTRIC POLARIZATION

When treating a periodic crystal, it is usual to work in terms of the dipole moment per unit volume, that is, the density of dipole moment, or polarization. Crystals whose symmetry allows an inversion center cannot present a net dipole moment.[17] For crystals without an inversion center, except point group 432,[18] certain deformations of the crystal lattice give origin to net dipole moments, known as the *piezoelectric* effect. In addition to this, the subset of those crystals that present an anisotropic direction in the lattice, called *polar*, are compatible with the existence of net dipoles even in the unstrained state, which is referred to as *spontaneous polarization*. The wurtzite (WZ) crystal structure belongs to the latter class and therefore WZ nitrides present both piezoelectric and spontaneous polarization.[17]

The piezoelectric response of a material to strain is modeled, in the linear regime,[19] via the piezoelectric tensor e_{ij}:

$$P_i^{\mathrm{pz}} = \sum_{j=1}^{6} e_{ij}\epsilon_j, \tag{1}$$

where P_i^{pz} are the components of the piezoelectric polarization vector and ϵ_j are the strains, given in Voigt notation.[20] The symmetry of the crystal determines the non-zero elements of e_{ij}. We shall see further on that, even for a bulk binary compound, one can define a *local* piezoelectric tensor e_{ij}^* whose *average* over the unit cell reduces to e_{ij}, but that has in general more nonzero elements than e_{ij}. The total polarization vector is given by

$$P_i = P_i^{\mathrm{sp}} + P_i^{\mathrm{pz}}, \tag{2}$$

where P_i^{sp} are the components of the spontaneous polarization vector, that will be present only if the crystal symmetry allows, as previously discussed.

Calculating the polarization of a periodic crystal might seem at first a trivial problem, with a possible intuitive definition being given by the charge density of the unit cell. However, there is no way of unambiguously defining the polarization vector using such a method, with an array of possible values arising from different choices of origin.[21] A rigorous frame for the computation of polarization in periodic solids was not available until as recently as the 1990s. The main developments were presented in the seminal papers by Vanderbilt and King-Smith,[22,23] building up on an idea originally suggested by Resta,[24] where the foundations of the *Berry-phase* theory of polarization, or *modern theory of polarization*,[25] were laid. This theory allows a calculation of the dipole moment of the unit cell of a periodic insulating system, which is well defined modulo $e\mathbf{R}$ (where e is the elementary charge and $\mathbf{R}$ is a lattice vector). The latter ambiguity can be removed in different ways, such that a meaningful value for the polarization can be obtained.[22,23,26] However, the obtainment of a position-dependent polarization vector, that varies *within* the unit cell in which the Berry phase is computed, is beyond the reach of this technique. Nevertheless, for systems where composition and/or strain change abruptly within the unit cell (e.g., random alloy InGaN QWs), the question of whether a local value of the polarization vector can be calculated becomes pertinent.

In the context of the Berry-phase technique, only the average polarization of the periodic unit cell as a whole can be calculated *formally*. In a general calculation, there may not necessarily be an obvious or straightforward way to partition the system into subsets for which the polarization can be easily computed in separate calculations. Any knowledge of how the polarization varies within the supercell must therefore rely on a heuristic assumption. This motivates to find a phenomenological solution to the problem, to gain access to physical information which would not be accessible otherwise. We show below that, within the present local polarization formalism, a position-dependent polarization, defined down to the unit volume of an ensemble of nearest neighbors, yields results in good agreement with a *formal* Berry-phase calculation, when extrapolated to calculate the average polarization of the supercell. This agreement provides strong support that the approach presented here provides an accurate description of local polarization effects in III-N heterostructures and alloys.

A. Formal definition of the local polarization

As already discussed, the total macroscopic polarization has two components: spontaneous and piezoelectric. Because the spontaneous polarization is a reference state, establishing a local value for it formally might prove rather nontrivial: one would need to devise an adiabatic transformation which keeps the system insulating while moving from an equivalent centrosymmetric structure to the polar crystal structure that allows to evaluate the difference in polarization locally (at each atomic site).[21] Therefore, to avoid this complexity, we assume the spontaneous polarization for a given binary compound to be position-independent and direct our attention towards the piezoelectric polarization instead.

Our aim is a reformulation of Eq. (1) that allows an evaluation of the local and macroscopic contributions to the polarization separately. For the sake of clarity and conciseness, we constrain ourselves to changes in P_i^{pz} that are linear in the strains. Future work will extend our description to second-order piezoelectric polarization. As we will see later on, the linear approximation breaks down quickly for some III-Vs but is good up to moderate strain for the highly

ionic III-nitrides. In analogy to elasticity,[27] we can generalize Eq. (1) for arbitrary internal strains as follows:

$$P_i^{\mathrm{pz}} = \sum_{j=1}^{6} e_{ij}\epsilon_j + \sum_{\alpha=1}^{N_{\mathrm{atoms}}} \sum_{k=1}^{3} \underbrace{\frac{\partial P_i^{\mathrm{pz}}}{\partial t_k^\alpha}}_{e\mathcal{Z}_{ik}^\alpha/V} \left[t_k^\alpha - t_{k,0}^\alpha(\boldsymbol{\epsilon})\right], \tag{3}$$

where N_{atoms} is the number of atoms in the unit cell, t_k^α is the kth component of the internal strain vector for atom α, e is the elementary charge, V is the volume of the unit cell, and $\mathcal{Z}_{ik}^\alpha$ is the ik component of the Born effective charge tensor[28] for atom α. $t_{k,0}^\alpha(\boldsymbol{\epsilon})$ are the internal strains that minimize the total energy of the crystal for any given strain state $\boldsymbol{\epsilon}$.[27] Although Eq. (3) is general, because we are working in the linear approximation we will assume that the off-diagonal components of the Born effective charges are zero. Equation (3) therefore reduces to

$$P_i^{\mathrm{pz}} = \sum_{j=1}^{6} e_{ij}\epsilon_j + \sum_{\alpha=1}^{N_{\mathrm{atoms}}} \frac{e\mathcal{Z}_i^\alpha}{V}\left[t_i^\alpha - t_{i,0}^\alpha(\boldsymbol{\epsilon})\right], \tag{4}$$

where we have employed an implicit notation $\mathcal{Z}_i^\alpha \equiv \mathcal{Z}_{ii}^\alpha$. Again, in the linear limit, the $t_{i,0}^\alpha$ are linear in $\boldsymbol{\epsilon}$ and we can write

$$P_i^{\mathrm{pz}} = \sum_{j=1}^{6} \underbrace{\left(e_{ij} - \sum_{\alpha=1}^{N_{\mathrm{atoms}}} \frac{e\mathcal{Z}_i^\alpha}{V}\frac{\partial t_{i,0}^\alpha}{\partial \epsilon_j}\right)}_{e_{ij}^{(0)}} \epsilon_j + \sum_{\alpha=1}^{N_{\mathrm{atoms}}} \frac{e\mathcal{Z}_i^\alpha}{V} t_i^\alpha, \tag{5}$$

where $e_{ij}^{(0)}$ is the piezoelectric coefficient obtained from a "clamped-ion" calculation,[26] in which the ionic coordinates are not allowed to relax. Note that in Eq. (5), the first term $e_{ij}^{(0)}$ is macroscopic, that is, defined for the unit cell as a whole, while the second one is evaluated locally.

Consider now that V_0 is the volume comprising an atomic site and all of its nearest neighbors (in the context of the four-fold coordinated ZB and WZ lattices this would correspond to each of the tetrahedra that make up the crystal). We label the central atomic site 0 and each of its nearest neighbors by $\alpha = 1,2,3,\ldots,N_{\mathrm{coor}}^0$. Then, the relevant quantity in Eq. (5) to be evaluated locally (at the atomic site 0) is

$$P_{i,\mathrm{local}}^{\mathrm{pz}}(0) \equiv \frac{e}{V_0}\left(\mathcal{Z}_i^0 t_i^0 + \sum_{\alpha=1}^{N_{\mathrm{coor}}^0} \frac{\mathcal{Z}_i^\alpha}{N_{\mathrm{coor}}^\alpha} t_i^\alpha\right), \tag{6}$$

where N_{coor}^α is the number of nearest neighbors of atom α. By dividing the contribution of each of the nearest neighbors $\mathcal{Z}_i^\alpha$ by their own number of nearest neighbors N_{coor}^α we ensure no double counting when extending the evaluation of Eq. (6) to the whole crystal.

The internal strains can be obtained in a relatively straightforward manner for binary compounds.[27,29] However, for an irregular material, such as an alloy, establishing a reference lattice structure with respect to which the internal strains could be calculated would carry a high degree of arbitrariness. Furthermore, an *exact* evaluation of Eq. (6) would rely on knowing the value of $\mathcal{Z}_i^\alpha$ for all the atoms present in the crystal. For an irregular material, $\mathcal{Z}_i^\alpha$ would differ, in general, for each atom, even (by a small amount) for atoms of the same species. Therefore our choice is to deduce an approximation to Eq. (6) valid for a representative reference system (such as a binary), and use that approximation to estimate the local polarization in irregular systems. We propose the following spherical approximation for the local environment of the central atom (atomic site 0):

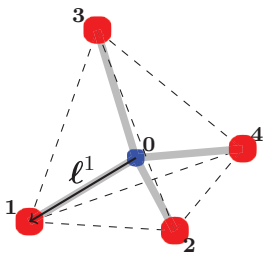

FIG. 1. (Color online) First nearest-neighbor environment in a tetrahedrally bonded crystal. The vector pointing from atom 0 (the central atom) towards atom α is denoted $\boldsymbol{\ell}^\alpha$.

$$\sum_{\alpha=1}^{N_{\mathrm{coor}}^0} \frac{\mathcal{Z}_i^\alpha}{N_{\mathrm{coor}}^\alpha} t_i^\alpha \approx -\frac{\mathcal{Z}_i^0}{N_{\mathrm{coor}}^0} \sum_{\alpha=1}^{N_{\mathrm{coor}}^0} t_i^\alpha. \tag{7}$$

The approximation given by Eq. (7) would be exact if all the nearest neighbors ($\alpha = 1,2,3,\ldots,N_{\mathrm{coor}}^0$) of atom 0 were piezoelectrically equivalent, that is, if all of them have the same Born effective charges. This is the case for binary ZB and WZ compounds. Further on, we will deal with how different approximations work out for alloys.

We can characterize the bonds between atom 0 and atoms $\alpha = 1,2,3,\ldots,N_{\mathrm{coor}}^0$ by a vector $\boldsymbol{\ell}^\alpha$ as indicated in Fig. 1. If $\boldsymbol{\ell}_0^\alpha$ is the bond vector of the unstrained case, we can write $\boldsymbol{\ell}^\alpha$ in terms of the macroscopic and internal strains:

$$\ell_i^\alpha = \sum_{j=1}^{3} (\delta_{ij} + \epsilon_{ij})\ell_{j,0}^\alpha + t_i^\alpha - t_i^0, \tag{8}$$

where ϵ_{ij} are the components of the strain tensor in Cartesian notation and δ_{ij} is the Kronecker delta function. With the approximation of Eq. (7) and the definition given by Eq. (8) we rewrite Eq. (5) as

$$P_i^{\mathrm{pz}} = \sum_{j=1}^{6} e_{ij}^{(0)}\epsilon_j - \frac{e}{V_0}\frac{\mathcal{Z}_i^0}{N_{\mathrm{coor}}^0}\left[\underbrace{\sum_{\alpha=1}^{N_{\mathrm{coor}}^0} \ell_i^\alpha}_{\mu_i} - \sum_{j=1}^{3}(\delta_{ij} + \epsilon_{ij})\underbrace{\sum_{\alpha=1}^{N_{\mathrm{coor}}^0} \ell_{j,0}^\alpha}_{\mu_{j,0}}\right], \tag{9}$$

where $\boldsymbol{\mu}$, defined as a summation over nearest-neighbor distances, is the *bond asymmetry parameter*.[4] $\boldsymbol{\mu}_0$ is the bond asymmetry parameter of the unstrained system, that would be zero for binary ZB materials and would have a nonzero component along the polar axis $\mu_{3,0}$ for WZ materials.[4]

Finally, we write for the *total* polarization at atomic site 0:

$$P_i = \underbrace{\sum_{j=1}^{6} e_{ij}^{(0)} \epsilon_j}_{\text{macroscopic}} + \underbrace{P_i^{\text{sp}} - \frac{e}{V_0}\frac{\mathcal{Z}_i^0}{N_{\text{coor}}^0}\left[\mu_i - \sum_{j=1}^{3}(\delta_{ij}+\epsilon_{ij})\mu_{j,0}\right]}_{\text{local}}. \quad (10)$$

Equation (10) is a central result of this paper, which separates the contributions to the polarization arising from macroscopic effects, given by the clamped-ion piezoelectric coefficient $e_{ij}^{(0)}$, and local effects, dominated by internal strain.

B. Validity of the model

We have made a number of approximations in the previous section. Depending on the nature of the compound at hand, each of them will have a different impact on the results, and will limit the accuracy that can be achieved. These approximations are the following. (1) We have assumed that $\mathbf{P}_{\text{sp}}$ is constant throughout the crystal for binaries. However, we have defined it as a *local* quantity (this will prove helpful when dealing with alloys). (2) For the piezoelectric part, we have truncated our description to first order in both macroscopic and internal strain. (3) We have assumed that the off-diagonal terms of the Born effective charge tensor are zero. (4) We have performed a spherical approximation for the Born effective charge of the nearest neighbors of the atom where the local polarization is evaluated.

As discussed in Sec. II A, it is not trivial to establish whether approximation (1) is good or not. It is possible to separate the contributions to $\mathbf{P}_{\text{sp}}$ into that arising from the *initial* bond asymmetry parameter $\boldsymbol{\mu}_0$ that we have defined previously (which in WZ is related to the internal parameter u), and the purely electronic contribution of the *ideal* WZ lattice.[4,30,31] In this context, it is possible to assign a local value for the initial bond asymmetry contribution, which in the case of WZ would be equal in both cation and anion sites. It seems therefore that assuming the electronic part to be also constant between different atomic sites for the binaries might be reasonable.

Approximation (2) is indeed the main limitation to the model introduced here, but possibly the most straightforward one to overcome. The theory can be extended to include second-order piezoelectric effects at the expense of complicating the formulas. We opt here to limit ourselves to a first-order description to emphasize the conceptual implications of the theory. The linear limit should be valid for highly ionic compounds, such as group-III nitrides, as will be shown in the next section. For the nitrides, although the second-order effects are large, the first-order terms dominate up to strain values that are typically found in realistic alloys and heterostructures (up to 5%).[1,10,32,33] However, for other III-V materials, second-order piezoelectric coefficients are relatively much larger compared to the linear ones. For instance, for the Al compounds AlP, AlAs, and AlSb, Beya-Wakata *et al.*[3] found that the first-order piezoelectricity can practically be neglected and second-order effects dominate even for small strains. For GaAs, the situation is intermediate and the present level of theory should be accurate for small strains below 1 or 2%. This complication is also present when computing the Born effective charges. As we show in Fig. 2 for the hydrostatic and biaxial strain dependence of $\mathcal{Z}$ (see the figure caption and next section for details of the calculation), the linear approximation for the Born effective charge gets worse as one moves from highly ionic AlN to the less ionic materials GaAs and AlAs. Note that strain-dependent Born effective charges also have an impact on the clamped-ion piezoelectric coefficient, as given by Eq. (5). Therefore a more complete and accurate treatment for general materials should eventually include the dependence of the Born effective charge $\mathcal{Z}_i$ on strain. Note that within this linear model, the contributions of clamped-ion terms and Born effective charges are assumed linear in the strains in the formal derivation of the formulas. However, the formalism does not *impose* a linear dependence of internal strain upon macroscopic strain when calculating the μ_i: this dependence is determined by the specific theoretical framework used for the computation of the atomic geometry of the system, e.g., DFT, a valence force field, etc. In the case

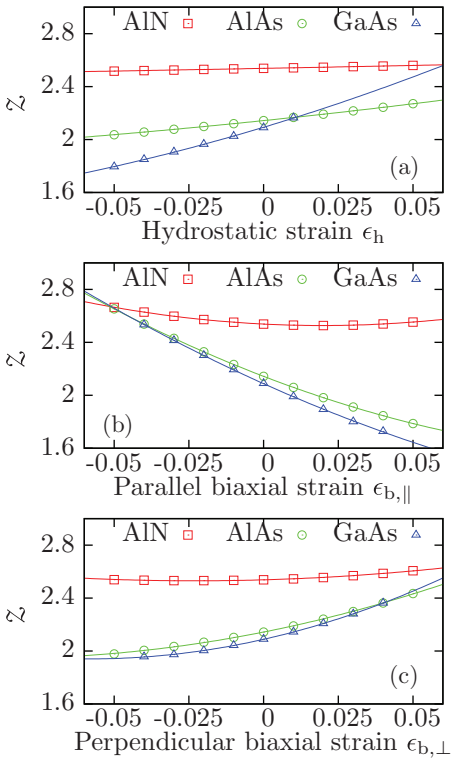

FIG. 2. (Color online) Born effective charges of the corresponding cation for ZB AlN, AlAs, and GaAs, as a function of (a) hydrostatic and (b) and (c) biaxial strain. "Parallel biaxial strain" means that the inequivalent strain axis coincides with the axis along which the Born effective charge is calculated, that is $\epsilon_1 = \epsilon_2 = \epsilon_{b,\parallel}$, $\epsilon_3 = -2\epsilon_{b,\parallel}$, and $\mathcal{Z} \equiv \mathcal{Z}_3$. "Perpendicular biaxial strain" refers to the opposite situation: $\epsilon_2 = \epsilon_3 = \epsilon_{b,\perp}$, $\epsilon_1 = -2\epsilon_{b,\perp}$, and $\mathcal{Z} \equiv \mathcal{Z}_3$. Open symbols are the results of LDA-DFT calculations (see Sec. II C for details) while solid lines are quadratic fits to the data. The missing points for GaAs within this strain range cannot be calculated because the LDA predicts a conducting state which is not compatible with the Berry-phase formalism (see discussion for InN in Sec. II C).[22,23]

of nitrides, Prodhomme *et al.*[33] have found relatively large nonlinear effects on binary and ternary compounds. As will be shown in the next section, the present local model succeeds at computing the polarization in nitride ternaries because its main non-linear contribution arises from nonlinearities of local internal strain *itself*, including the effect of disorder.

Approximation (3) is generally good, since for binary compounds the off-diagonal components of the Born effective charge are typically zero, and in any case the ratio $\mathcal{Z}_{ij}/\mathcal{Z}_{ii}$ $(i \neq j)$ is usually small.

The validity of approximation (4) relies greatly on the specific crystalline structure and whether the nearest neighbors of the central atom where the polarization is being calculated are equivalent (that is, have the same Born effective charge) or not. For this reason, in the case of binary tetrahedrally bonded compounds, where all the nearest neighbors for one given site are of the same atomic species, this approximation should be good for small strains. As observed in Fig. 2 for biaxial strain, lattice distortions that change the symmetry of the bonds have a large impact on the Born effective charge for some compounds. Therefore the validity of Eq. (10) would be limited for low ionicity and the more general form, Eq. (5), should be used. On the other hand, for ionic compounds such as nitrides, Eq. (10) retains its validity and offers an accurate description of the local effects, as will be shown in Sec. II C. In both cases (low and high ionicity in tetrahedrally bonded binaries), the approximation is exact for the linear piezoelectric limit (see Sec. II C2).

C. Testing the theory for group-III nitrides

As a first validation test and application of the theory, we have chosen group-III nitrides. The III nitrides are technologically important semiconductors for a wide range of optoelectronic applications.[34–36] The strong piezoelectric response of nitride compounds, together with the existence of the spontaneous polarization, has a large impact on the electromechanical properties of devices that incorporate them. The large difference in bond lengths between the nitride binaries leads to considerable local strains in these alloys, with measurable effects such as large band-gap bowings.[37,38] We have previously shown how these local strain fields affect the electric polarization for InGaN alloys, retrieving the macroscopic limit with the advantage of giving a description of the local effects at the same time.[4] We have now presented in Sec. II a refined and more general form of that model. In the following, we will thoroughly apply this theory to test its validity for III-N materials.

1. Parameters involved in the calculation of the local polarization

The first step in setting up the theory is to derive the necessary parameters for the WZ III-N binaries GaN, AlN, and InN: piezoelectric tensor e_{ij}, spontaneous polarization P_i^{sp}, Born effective charges $\mathcal{Z}_i$, lattice parameters a_0 and c_0, internal parameter u_0, and internal strain parameters ζ_i. For our calculations, we have used the plane wave implementation of density functional theory (DFT) available from the VASP package,[39,40] within the projector augmented-wave (PAW) method.[41,42] We perform calculations using both the local density approximation (LDA) and the Heyd-Scuseria-Ernzerhof (HSE) screened-exchange hybrid functional.[29,43,44] For the LDA calculations, we use VASP's implementation of the Perdew-Zunger parametrization,[45] while the settings for the HSE functional correspond to HSE06, with mixing parameter $\alpha = 0.25$ and screening parameter $\mu = 0.2$. In all calculations, the cutoff energy for plane waves is 600 eV. All the quantities involving a calculation of the polarization have been obtained using Martijn Marsman's implementation of the Berry-phase technique[23] available in VASP. We use HSE to obtain high-quality parameters for the binaries and LDA to perform test calculations for larger supercells and for statistical evaluation of the accuracy of the theory. In our experience, LDA-DFT gives a good description of elastic properties and internal strain, while at the same time being computationally affordable. Also, LDA-DFT seems to give results in better agreement with experiments than generalized-gradient approximations (GGAs) for the calculated electric polarization, at least for III-V compounds.[3] The more computationally demanding HSE functional, on the other hand, reduces the band-gap problem existent in standard Kohn-Sham DFT,[46] that potentially leads to a conducting phase being incorrectly predicted for narrow gap semiconductors, such as InN. HSE also provides lattice parameters and elastic properties in better agreement with experiment.[29]

The calculated structural and polarization-related parameters of the III-N binaries are summarized in Table I. In the context of the Berry-phase approach, a meaningful value for the polarization can only be calculated if the system remains insulating.[22,23,25] As already discussed, in the case of the III-N compounds this is not a problem for the HSE functional, which predicts a positive gap.[47] Using the LDA, AlN and GaN are predicted to have (underestimated) positive gaps. However, our settings lead to the prediction of a band crossing at the Γ point for InN, and therefore an incorrect metallic phase that renders the calculation of a meaningful value of the polarization uncertain. Previous data have been given for InN by Fiorentini and collaborators in a series of papers on the piezoelectric properties and spontaneous polarization of group-III nitrides.[26,30,48] While their LDA calculations obtain the correct insulating phase of InN,[49] ours must rely on a different approach. Because the band crossing occurs only at the Γ point and immediate surroundings, we skip this area in the k-point integration by shifting the $\mathbf{k}$ mesh away from Γ. The resulting LDA values of the polarization-related quantities in Table I show almost perfect agreement with Fiorentini *et al.*'s LDA data,[30,48] although InN remains technically a metal in our case. The good agreement with the HSE calculation further supports that our LDA values should be correct.

It should be noted that our calculations yield a negative sign for e_{15} in both the LDA and HSE schemes. Initial measurements[50] and calculations[51] reported a positive value for e_{15}, as included in Vurgaftman and Meyer's widely cited review paper.[52] Our value here is in line with more recent studies and analyses which show that a negative value is required both for agreement with experiment and for internal consistency among the different piezoelectric coefficients.[6,53–55] Very recent LDA calculations of second-order polarization of III-nitrides and ZnO by Prodhomme *et al.*[33] show good agreement with our linear coefficients of Table I. The agreement between HSE and LDA highlights

TABLE I. Parameters involved in the calculation of polarization-related quantities for WZ group-III nitrides, obtained from DFT calculations as explained throughout the text. The HSE lattice parameters a_0, c_0, internal parameter u_0, and internal strain parameters ζ_i are taken from Ref. 29. The **k** grids are $6 \times 6 \times 4$ Γ-centered for a four-atom hexagonal cell in all cases except for the calculation of e_{ij}, $e_{ij}^{(0)}$, P^{sp} and $\mathcal{Z}_i$ for InN in the LDA scheme. For those quantities, we use an orthorhombic-equivalent 16-atom supercell and the sampling in k space is $4 \times 4 \times 4$, following the standard Monkhorst-Pack scheme implemented in VASP, which does not include Γ in the integration (see text for details).[39] Note that in all cases, the positive sign for $\mathcal{Z}_i$ implies a displacement of the cation sublattice: the corresponding Born effective charge of the anions is $-|\mathcal{Z}_i|$. $P^{\mathrm{sp}}_{\mathrm{idWZ}}$ is the spontaneous polarization of the ideal WZ lattice (lattice parameters and internal parameter extrapolated from the ZB phase).

	AlN		GaN		InN	
	HSE	LDA	HSE	LDA	HSE	LDA
a_0 (Å)	3.103	3.092	3.180	3.154	3.542	3.507
c_0 (Å)	4.970	4.947	5.172	5.141	5.711	5.668
u_0	0.3818	0.3820	0.3772	0.3765	0.3796	0.3787
ζ_1	0.138	0.145	0.156	0.168	0.193	0.204
ζ_2	0.086	0.091	0.083	0.089	0.107	0.112
ζ_3	0.191	0.200	0.159	0.168	0.218	0.226
ζ_4	0.199	0.224	0.201	0.210	0.337	0.339
ζ_5	0.143	0.140	0.141	0.148	0.107	0.118
e_{15} (C/m^2)	−0.39	−0.43	−0.32	−0.36	−0.42	−0.47
e_{31} (C/m^2)	−0.63	−0.69	−0.44	−0.49	−0.58	−0.63
e_{33} (C/m^2)	1.46	1.59	0.74	0.83	1.07	1.09
P_3^{sp} (C/m^2)	−0.091	−0.096	−0.040	−0.029	−0.049	−0.041
$P^{\mathrm{sp}}_{3,\mathrm{idWZ}}$ (C/m^2)	−0.031	−0.033	−0.019	−0.016	−0.019	−0.016
$e_{15}^{(0)}$ (C/m^2)	0.28	0.28	0.43	0.45	0.39	0.35
$e_{31}^{(0)}$ (C/m^2)	0.26	0.25	0.40	0.41	0.37	0.38
$e_{33}^{(0)}$ (C/m^2)	−0.51	−0.47	−0.87	−0.87	−0.87	−0.95
$\mathcal{Z}_1(=\mathcal{Z}_2)$	2.53	2.52	2.64	2.58	2.85	2.83
$\mathcal{Z}_3$	2.68	2.67	2.77	2.72	3.02	3.00

the fact that LDA provides reliable values for the electric polarization provided that it also succeeds at predicting reliable band gaps and structural parameters: the largest discrepancies are for the spontaneous polarization of GaN and InN, which are influenced by the discrepancy between HSE and LDA for the calculated value of u_0.

2. *Local piezoelectric tensor*

We have previously obtained the relation between macroscopic and internal strain for the WZ lattice and provided the definition of the five WZ internal strain parameters ζ_i in Ref. 29. To obtain the relation between piezoelectric coefficients e_{ij} and internal strain parameters ζ_i, one can apply Eq. (5) to the internal strain vectors for the WZ geometry. The results can conveniently be expressed in the following compact form:

$$\begin{aligned} e_{15} &= e_{15}^{(0)} - \frac{2e\mathcal{Z}_1}{\sqrt{3}{a_0}^2}\zeta_1, \\ e_{31} &= e_{31}^{(0)} - \frac{4e\mathcal{Z}_3}{\sqrt{3}{a_0}^2}\zeta_2, \\ e_{33} &= e_{33}^{(0)} + \frac{4e\mathcal{Z}_3}{\sqrt{3}{a_0}^2}\zeta_3. \end{aligned} \tag{11}$$

We have incorporated in Eq. (11) none of the assumptions leading to Eq. (10). Therefore Eq. (11) is an exact result for WZ crystals in a linear piezoelectric model. It is thus initially surprising that ζ_4 and ζ_5, although breaking the cell symmetry, do not appear in the expressions for the e_{ij}. The reason for this will become clear when obtaining the e_{ij} as $\frac{\partial P_i}{\partial \epsilon_j}$, calculated from Eq. (10). Following the convention of Fig. 3, the *local* piezoelectric tensor, notated e^*_{ij}, can be calculated at the atomic sites A and C, corresponding to the two cations present in the unit cell, as the derivative of Eq. (10) with respect to the strains:

$$e^{*,X}_{ij} = e^{(0)}_{ij} - \frac{e\mathcal{Z}^X_i}{\sqrt{3}{a_0}^2 c_0}\left(\frac{\partial \mu^X_i}{\partial \epsilon_j} - \sum_{k=1}^{3}\frac{\partial \epsilon_{ik}}{\partial \epsilon_j}\mu^X_{k,0}\right), \tag{12}$$

where X indicates A or C. For a WZ structure, the only nonzero component $\mu_{k,0}$ is $\mu_{3,0} = 4(u_0 - 3/8)c_0$.[4] Expressing $\boldsymbol{\mu}$ in terms of macroscopic strains, lattice parameters and internal strain parameters, each of the nonzero components of e^*_{ij}

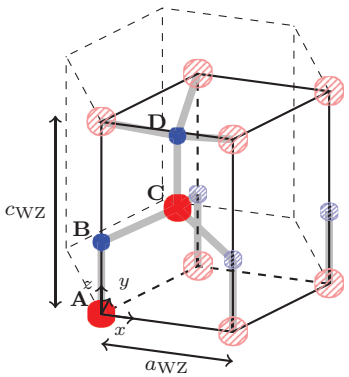

FIG. 3. (Color online) Standard four-atom WZ unit cell. A and C are cations, B and D are anions.

can be obtained (an example calculation for $e_{15}^{*,\mathrm{A}}$ is given in Appendix A):

$$\begin{aligned}
e_{15}^{*,\mathrm{A}} &= e_{15}^{*,\mathrm{C}} = e_{15}^{(0)} - \frac{2e\mathcal{Z}_1}{\sqrt{3}{a_0}^2}\zeta_1,\\
e_{16}^{*,\mathrm{A}} &= -e_{16}^{*,\mathrm{C}} = \frac{\sqrt{3}e\mathcal{Z}_1}{2a_0c_0}\zeta_4 + \frac{e\mathcal{Z}_1}{\sqrt{3}{a_0}^2}\zeta_5,\\
e_{21}^{*,\mathrm{A}} &= -e_{21}^{*,\mathrm{C}} = e_{16}^{*,\mathrm{A}},\\
e_{22}^{*,\mathrm{A}} &= -e_{22}^{*,\mathrm{C}} = -e_{16}^{*,\mathrm{A}},\\
e_{31}^{*,\mathrm{A}} &= e_{31}^{*,\mathrm{C}} = e_{31}^{(0)} - \frac{4e\mathcal{Z}_3}{\sqrt{3}{a_0}^2}\zeta_2,\\
e_{33}^{*,\mathrm{A}} &= e_{33}^{*,\mathrm{C}} = e_{33}^{(0)} + \frac{4e\mathcal{Z}_3}{\sqrt{3}{a_0}^2}\zeta_3.
\end{aligned} \tag{13}$$

That is, the expressions for e_{15}, e_{31} and e_{33} are retrieved exactly, but additional piezoelectric components appear, that change sign going from A to C. To elucidate the effect of this on the symmetry of the piezoelectric tensor, we write e_{ij}^{*} in matrix form:

$$e_{ij}^{*,\mathrm{A/C}} \equiv \begin{pmatrix} 0 & 0 & 0 & 0 & e_{15} & \pm e_{16}^{*} \\ \pm e_{16}^{*} & \mp e_{16}^{*} & 0 & e_{15} & 0 & 0 \\ e_{31} & e_{31} & e_{33} & 0 & 0 & 0 \end{pmatrix}. \tag{14}$$

When averaging $e_{ij}^{*,\mathrm{A}}$ and $e_{ij}^{*,\mathrm{C}}$ within a given unit cell, one retrieves the WZ macroscopic limit:

$$\frac{1}{2}\left(e_{ij}^{*,\mathrm{A}} + e_{ij}^{*,\mathrm{C}}\right) \equiv \begin{pmatrix} 0 & 0 & 0 & 0 & e_{15} & 0 \\ 0 & 0 & 0 & e_{15} & 0 & 0 \\ e_{31} & e_{31} & e_{33} & 0 & 0 & 0 \end{pmatrix}. \tag{15}$$

The anion sites B and D have the same expressions for e_{15}, e_{31} and e_{33} and slightly different expressions for e_{16}^{*}:

$$e_{16}^{*,\mathrm{B}} = -e_{16}^{*,\mathrm{D}} = -\frac{\sqrt{3}e\mathcal{Z}_1}{2a_0c_0}\zeta_4 - \frac{2e\mathcal{Z}_1}{\sqrt{3}{a_0}^2}\zeta_5. \tag{16}$$

The macroscopic limit is of course also retrieved when averaging for the anion sites. Note that the values of e_{16}^{*} are comparable to those of the macroscopic piezoelectric tensor coefficients. For instance, for GaN, $|e_{16}^{*}|$ amounts to 0.79 and 1.13 C/m^2 for cation and anion sites, respectively.

Equation (14) is the (site-dependent) local piezoelectric tensor for a WZ lattice. It reflects the fact that there exist two sets of inequivalent tetrahedra in a WZ lattice, and that the macroscopic strain affects the nearest-neighbor environment of each of them differently.[27,29] This is *a priori* an unexpected result, and implies that crystals that are non-polar and non-piezoelectric *on average* could nevertheless present a local, perhaps measurable, piezoelectric-like polarization.

Finally, note the similarity between the local piezoelectric tensor of WZ and that of ZB in a (111)-oriented description [see Eq. (27) of Ref. 6]. This reflects that (111)-oriented ZB systems present a threefold symmetry,[6] where all cation (anion) sites have an equivalent environment, contrary to the WZ case, where there are two inequivalent cation (anion) sites.[29]

3. *Local polarization in InGaN alloys: strategies and testing*

We have seen so far that for wurtzite nitride binaries there is an exact correspondence between local and macroscopic polarization that is retrieved when averaging the local part over the unit cell. Although some solid-state devices might operate employing binary compounds, the most interesting applications of the nitrides arise through the use of their alloys for controlled variation of properties (e.g., band-gap tunability).

The main problem facing a local polarization calculation for an alloy is the increased complexity of the atomic environment of each of the sites where the local polarization is to be evaluated. This is due to the fact that the Born effective charges of all the atoms involved in the calculation are affected by the interaction with all the other atoms present in the crystal. In a periodic cell calculation, this number would be reduced to the number of atoms in the supercell. Since there is an arbitrarily large number of possible configurations depending on alloy composition and supercell size, establishing an exact correspondence between local and macroscopic polarization in the fashion of Sec. II A then becomes virtually impossible. To overcome this limitation, we will assume for the nitrides, and InGaN in particular, that the Born effective charge of the cations in the alloy remains the same as for the binary, and that the spherical approximation still holds.[4] We have devised two tests in order to establish how good this approximation is. First, we will use the smallest alloy cell, which is a CuPt-like (CP-like) InGaN unit cell consisting only of four atoms,[4,30] and will perform random distortions of the atomic positions within the unit cell. The result of the averaged local polarization, calculated using Eq. (10), will be compared to the formal Berry-phase result. Second, 32- and 128-atom $In_{0.5}Ga_{0.5}N$ supercells will be considered and the cation sites occupied randomly with either a Ga or an In atom, with the only requirement that the stoichiometric ratio of 1/1 be preserved (i.e. the nominal composition of all cells is the same). The internal atomic positions will then be allowed to relax by minimizing the supercell LDA-DFT total energy, and the result of the averaged local polarization will again be compared to that of a Berry-phase calculation. The statistical treatment of both tests will reveal the validity of the approximation for InGaN alloys.

The results of the first test are depicted in Fig. 4. The figure shows a comparison of the average polarization of the CP-like InGaN cell calculated both within the present local polarization model and with the Berry-phase technique. We have performed random displacements of up to ± 0.2 Å (which is equivalent to approximately 10% of the equilibrium bond lengths) to each of the Cartesian coordinates of each of the four atoms in the unit cell. For the local polarization model, we have computed the local polarization contributions at the Ga and In sites using Eq. (10) and then obtained its average for the whole cell. Since only differences in polarization are meaningful within the Berry-phase formalism,[22,23] we compare in Fig. 4 the difference ΔP between the polarization of the equilibrium CP-like InGaN structure and the distorted one. As can be seen, the agreement between the two methods is excellent, with all the data points lining up against the dashed line that corresponds to perfect agreement $\Delta P_{\mathrm{model}} = \Delta P_{\mathrm{Berry\,phase}}$.

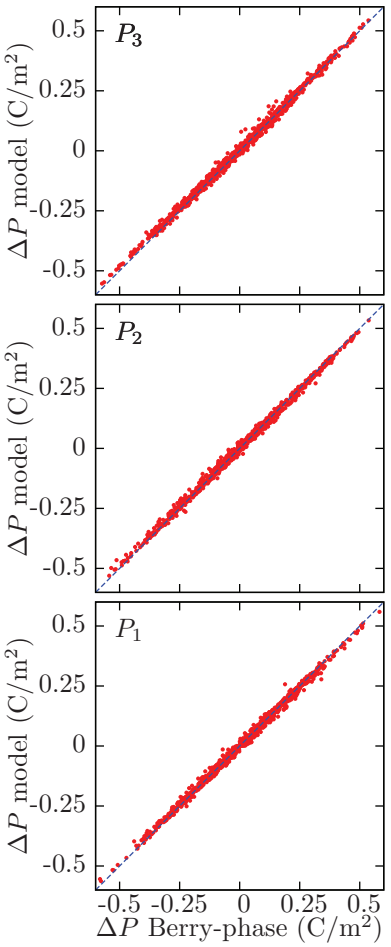

FIG. 4. (Color online) Comparison between the polarization predicted by the present model and a Berry-phase calculation for a large number (1000) of randomly distorted CP-like InGaN cells (four-atom unit cell). ΔP is the difference in polarization between the equilibrium and distorted structures, where the lattice vectors are fixed but the coordinates of each atom in the unit cell are varied randomly up to ± 0.2 Å in each Cartesian direction. The Berry-phase values are LDA-DFT results. The dashed line indicates perfect agreement between the two methods, that is $\Delta P_{\text{model}} = \Delta P_{\text{Berry-phase}}$. A few random distortions within the range lead to a metallic phase being predicted by LDA, and were left out of the comparison.

Even more enlightening is the comparison between the present model and the Berry-phase results depicted in Fig. 5 for random $In_{0.5}Ga_{0.5}N$ orthorhombic supercells. In that figure, ΔP is the difference between the polarization of the supercell before and after internal strain relaxation. The supercells are constructed with either 32 or 128 atoms and the In and Ga atoms are placed randomly at the cation sites. The lattice vectors of the supercells are kept fixed and chosen as the average between the LDA values for the binaries. The "site count" panels show the number of cation sites that present a particular *local* polarization value within different ranges, for the combined supercells. We note two main features. The first observation is that the local polarization model succeeds at very accurately predicting the average supercell polarization even though the latter is calculated from a sum over many local contributions whose values vary within limits which are approximately one order of magnitude higher. Second, our results show that the average polarization is highly dependent on the specific atomic arrangement, even for a large number of atoms. Bernardini and Fiorentini[30] have previously calculated the spontaneous polarization for the same material using a 32-atom special quasirandom structure (SQS),[56] and have proposed that disorder plays only a secondary role in the calculation of the polarization, both spontaneous and piezoelectric.[1,30,32,57] We have found that this is indeed the case for the spontaneous polarization of the supercells studied *before* the optimization of the atomic degrees of freedom: all the 128-atom configurations studied yielded the same value of ~ -0.009 C/m^2 within less than 0.001 C/m^2 of each other. However, our results suggest (i) that a 32-atom supercell might not be large enough to study the effect of disorder (see, e.g., clustering of calculated values for P_2 in Fig. 5) and (ii) that internal strain relaxation introduces large corrections to the polarization value, even for supercells containing as many as 128 atoms. Note, for instance, that the average in-plane components of the polarization P_1 and P_2, which are not symmetry-allowed for the binaries, do not vanish for the alloys in the case of finite-size supercells. All of these considerations not only support the validity of the local model discussed here, but also highlight the need for one, in order to be able to treat the effects of disorder and associated internal strain accurately.

III. POINT DIPOLE METHOD FOR THE CALCULATION OF THE POLARIZATION POTENTIAL

When trying to calculate the local polarization potential by solving Poisson's equation $\nabla \cdot (\varepsilon \nabla \phi) = \nabla \cdot \mathbf{P}$ in the same atomic grid where the polarization is given, one encounters two main difficulties. The first arises from the discretization of the medium, which is irregular given the arrangement of the atoms in the strained crystal. The second, and most important, is a problem of resolution: because Poisson's equation needs to be solved in a finite difference or polynomial interpolation schemes, and its solution involves the calculation of several derivatives (see, for instance, Ref. 58), approximate interpolations have to be made and the effects of abrupt local discontinuities are lost in the process. In order to compute the local polarization potential and overcome these limitations, we have previously used a point dipole model.[4] Here, we give the details of our model and extend it, as well as assess its limitations and degree of validity for calculations involving a position-dependent value of the polarization.

The point dipole model is a solution to the challenge of solving Poisson's equation on an atomic grid where abrupt changes in the polarization vector occur.[4] This is achieved with a method that computes at any arbitrary position the potential contribution due to each dipole individually, without involving the interpolation of quantities between neighboring grid sites that would lead to loss of resolution. However, before the polarization potential can be obtained from the point dipoles, a remapping of polarization density into dipole moment on the system's grid has to be performed. The latter is dealt with in Sec. III A. The general solution for the polarization potential arising from the ensemble of point dipoles is obtained in Sec. III B in an image dipole scheme, for a QW system (or layered structure, in general) where a different arbitrary

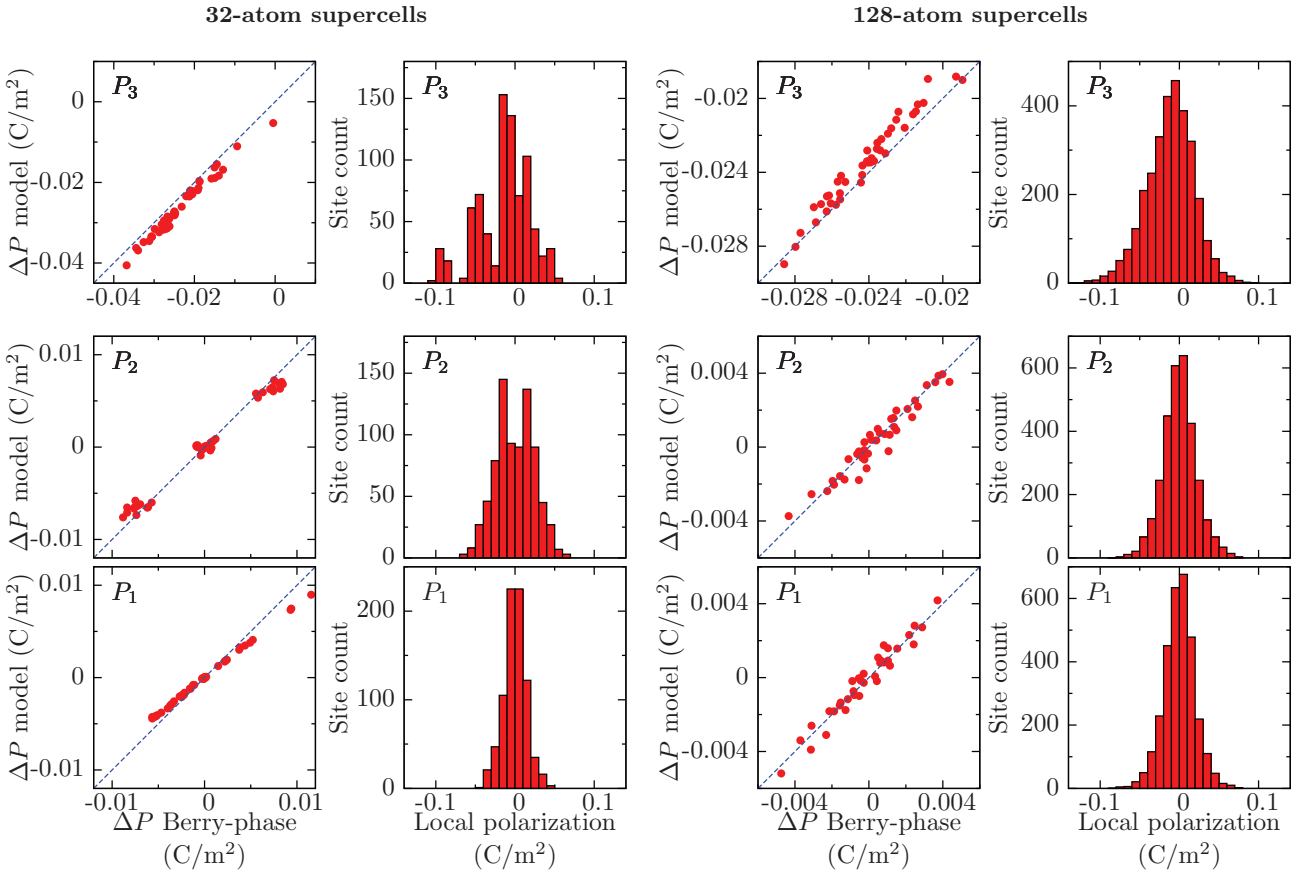

FIG. 5. (Color online) Comparison between the spontaneous polarization calculated using the present local model and the Berry-phase technique for a series of $In_{0.5}Ga_{0.5}N$ random supercells with 32 and 128 atoms. ΔP is the difference between the polarization of the supercells before and after internal strain relaxation. The Berry-phase values and the relaxed atomic positions are LDA-DFT results. The dashed line indicates perfect agreement between the two methods, that is $\Delta P_{\text{model}} = \Delta P_{\text{Berry phase}}$. The supercells are orthorhombic, with the lattice vectors given by the average of the InN and GaN lattice parameters. In terms of cation layers, the 32-atom supercells have a $2 \times 4 \times 2$ arrangement while the 128-atom supercells are $4 \times 4 \times 4$. The "site count" panels for each series refers to the number of cation sites that registered a local polarization value within the ranges shown (of width 0.01 C/m^2), for the combined supercells.

dielectric constant is allowed for all three neighboring layers of material. The effect of different levels of approximation for this general solution is also treated in Appendix B. In Sec. III C, we present a comparison between the solution of Poisson's equation for a problem with an available analytical solution and different levels of implementation of our method. Further material complementary to this section, including computational aspects, is given in Appendix B.

A. From polarization to dipole moment

Before establishing the form of the potential due to a point dipole ensemble, we focus our attention on the transformation between polarization density **P**, which is the quantity usually calculated in strained crystals, and dipole moment **p**, which is the quantity involved in the equations that will be presented in the next section.

The polarization **P** can be understood as a "density of dipole moment." Indeed, the total dipole moment of a finite size sample in which the polarization density is constant is simply the product of **P** and the volume of the sample. Therefore, when dealing with constant polarization in a continuum-based description, a standard cubic discretization of the material, with step size Δ, is well suited to the representation of **P** as an ensemble of dipoles of magnitude $\mathbf{p} = \mathbf{P}\Delta^3$ located at each of the mesh points. However, our main interest is the representation of the material as an ensemble of point dipoles in an atomistic scheme. For tetrahedrally bonded compounds this involves the discretization in a mesh with either cubic (zinc-blende) or hexagonal (wurtzite) coordination, in the ideally undistorted lattice. After strain is applied, the former grids will suffer a deviation from cubic and hexagonal symmetries and the assignment of a finite volume to each mesh point becomes cumbersome.

In the description of local polarization that we have previously employed, the values of **P** were given at the sites of each of the cations present in the crystal.[4] The latter is a useful description, in the sense that the representation of the whole crystal as a collection of deformed tetrahedra can be done via the relative positioning of the nearest neighbors: each cation and its four neighboring anions unambiguously define each tetrahedron. Labeling the anions immediately surrounding a cation as 1, 2, 3, and 4 (see Fig. 1), we refer to the volume of the corresponding tetrahedron as V_{1234}. If the positions of the

anions are $\mathbf{r}_1$, $\mathbf{r}_2$, $\mathbf{r}_3$ and $\mathbf{r}_4$, then V_{1234} is given by

$$V_{1234} = \tfrac{1}{6}|(\mathbf{r}_1 - \mathbf{r}_4) \cdot [(\mathbf{r}_2 - \mathbf{r}_4) \times (\mathbf{r}_3 - \mathbf{r}_4)]|. \quad (17)$$

However, it can be easily shown that V_{1234} only accounts for the volume of the tetrahedron itself and that a summation of the volumes of all the tetrahedra contained within a material sample would underestimate the volume of the sample by exactly a factor of 6. Therefore we define the volume *corresponding* to a tetrahedron as

$$\tilde{V}_{1234} = 6V_{1234}. \quad (18)$$

Now, the value of the dipoles can be easily obtained once a map of the polarization is available. For simplicity, we denote each grid point by i and the volume of the corresponding tetrahedron, as given by Eq. (18), as $\tilde{V}_i$:

$$\mathbf{p}_i = \mathbf{P}_i \tilde{V}_i, \quad (19)$$

with $\mathbf{p}_i$ being located at the position $\mathbf{r}_i$ of cation i.

Our choice for a cation-based description stems from convenience. In a nitride alloy, all the anions are nitrogen atoms and therefore applying the spherical approximation of Eq. (7) (which is based on nearest neighbors only) leads to one Born effective charge definition per cation atomic species: Ga, In, and Al for conventional III-N. Using an anion-based description would lead, in the case of nitrides, to defining 15 different Born effective charges for N, which correspond to the 15 possible combinations of Ga/In/Al atoms that can be nearest neighbors to N (e.g., four Ga, three Ga and one In, two Al and two In, etc.).

B. Solution for materials with different dielectric constant

Given the multipole expansion of a distribution of electric charge (see, for example, Ref. 59), the contribution to the electrostatic potential $\phi_{\mathbf{p}}$ calculated at $\mathbf{r}$ due to a point dipole $\mathbf{p}$ is given by

$$\phi_{\mathbf{p}}(\mathbf{r}) = \frac{1}{4\pi\varepsilon_0\varepsilon_r} \frac{\mathbf{p} \cdot (\mathbf{r} - \mathbf{r}_{\mathbf{p}})}{|\mathbf{r} - \mathbf{r}_{\mathbf{p}}|^3}, \quad (20)$$

where $\mathbf{r}_{\mathbf{p}}$ is the position of the dipole $\mathbf{p}$, ε_0 is the permittivity of the vacuum, and ε_r is the dielectric constant of the material. Equation (20) is only valid when both the dipole $\mathbf{p}$ at $\mathbf{r}_{\mathbf{p}}$ and the point $\mathbf{r}$ where the potential is calculated are contained within an infinite (or big enough to neglect surface effects) sample of a dielectric material with dielectric constant ε_r. For the more general case in which there are boundaries between materials with different dielectric constants, e.g., a quantum well, it is appropriate to use the method of images to obtain a form of Eq. (20) that accounts for the discontinuity of ε_r across the different interfaces. The details of the method and the treatment for the case of up to three material layers with different dielectric constants are given in Appendix B.

C. Comparison to the solution of Poisson's equation for simple structures

Before applying the model to calculate the local polarization potential in realistic structures, it is necessary to test its accuracy against well established methods. An excellent test is the calculation of the polarization potential in a capacitor-like structure. In such an example, a layer of dielectric material (1) of thickness h, in which the polarization $\mathbf{P} = P_0\,\hat{\mathbf{z}}$ (where $\hat{\mathbf{z}}$ is a unit vector along the z axis) is constant and perpendicular to the neighboring interfaces, is surrounded by two infinite layers of a dielectric material (2), with a different dielectric constant, in which the polarization is zero. An exact analytical solution to Poisson's equation can be obtained for the latter case. If we assume the first interface is located at $z = 0$, the potential is given by

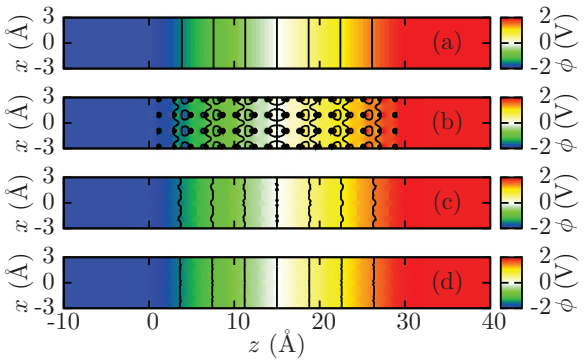

FIG. 6. (Color online) Potential obtained at different levels of approximation for a QW of width $h = 30$ Å for which $P_0 = 0.1$ C/m^2 and $\varepsilon_r = 8.4$. In the barrier, $P = 0$ and $\varepsilon_r = 9.6$. (a) Analytic solution [Eq. (21)], (b) direct application of the present dipole method, (c) dipole method with cutoff radius $r_{\text{cutoff}} = 1$ Å and (d) dipole method with Gaussian smearing implementation, $r_{\text{smear}} = 1.5$ Å and $\sigma = 1$ Å (see Appendix B).

$$\phi(\mathbf{r}) = \frac{P_0}{2\varepsilon_0\varepsilon_r^{(1)}}(|z| - |z - h|), \quad (21)$$

where $\varepsilon_r^{(1)}$ is the dielectric constant of material (1). Figure 6(a) shows the potential profile as calculated exactly and analytically using Eq. (21) for the special case in which $P_0 = 0.1$ C/m^2, $\varepsilon_r^{(1)} = 8.4$, and $h = 30$ Å, which would be typically the situation in an InGaN QW surrounded by GaN barriers in which, for simplicity, the polarization has been switched off in the barriers. Within this simplified continuum picture, a spatial discretization of the current problem in a cubic grid of steps $\Delta \approx 2$ Å, as discussed in the previous section, creates an ensemble of point dipoles, which are of similar size to the ones encountered in typical InGaN QW situations. The application of our dipole method to first-order reflections (see Appendix B) leads to a potential profile as in Fig. 6(b). In that figure, it can be observed how the potential changes brusquely in the surroundings of the dipoles (the plane of the figure has been deliberately chosen to be one that contains dipoles in it to dramatize this effect). This is due to the fact that Eq. (20) is a valid solution for a distribution of charge only if the position where the potential is calculated is sufficiently far away from the location of the point dipole that represents that distribution. We acknowledged this limitation in our previous work and proposed a cutoff radius around $\mathbf{r}$ for which only the dipoles that obey the condition $|\mathbf{r} - \mathbf{r}'| > r_{\text{cutoff}}$ are taken into account.[4] The potential profile for the present example and $r_{\text{cutoff}} = 1$ Å is shown in Fig. 6(c). Although this solution certainly improves the results and leads to a much better agreement with the analytical solution, it has the inconvenience of creating sharp transitions at the cutoff

distances around the dipoles. To complement this treatment, we have now substituted the elimination of dipoles below the cutoff radius by a Gaussian smearing of dipoles that obey the condition $|\mathbf{r} - \mathbf{r}'| < r_{\text{smear}}$, as detailed in Sec. B 2 of Appendix B. This solution leads to smoother potentials and a much better agreement with the analytic solution for this test case, as observed in Fig. 6(d).

IV. SELECTED RESULTS FOR InGaN QUANTUM WELLS

Once the method for calculating the local polarization potential has been established, we can turn our attention towards achieving a local description of that quantity in relevant nanostructures. In the present example, we look at InGaN/GaN QWs grown along polar and nonpolar[60] directions. Polar structures are grown along the c axis, whereas in the case of nonpolar structures the c axis lies within the growth plane. In a macroscopic picture of the polarization, there are no discontinuities in $\mathbf{P}$ between the well and barriers in the nonpolar case. However, as we shall see, in a microscopic description discontinuities occur locally, depending on local strain and composition.

Although we used in Sec. II C DFT to optimize the atomic positions of the supercells studied, such an approach is unaffordable for large supercells, given both the computer time and memory usage required. The usual approach to relax the atomic degrees of freedom in such cases is to use a classical interatomic force method. For tetrahedrally bonded compounds, Keating's valence force field (VFF) model[61] is by far the most popular.[62,63] Camacho and Niquet have previously used a modified version of Keating's model, adapted to the WZ crystal structure, to account for the deviation of the c/a ratio of lattice parameters with respect to its ideal value.[63] We have instead chosen an approach based on Martin's VFF[64] that includes the electrostatic interaction explicitly.[4] At a higher computational cost, this model succeeds at predicting the deviation of the c/a ratio while maintaining the correct symmetry of the interatomic interactions. For instance, the two-body interactions directed along the WZ c axis have the same functional form, including the equilibrium bond length, as the other ones. This allows to obtain a much more flexible set of potentials that are transferable between similar polymorphs of the same compound, i.e., WZ and ZB in this case. With our model we are able to predict elastic and structural properties of binary and ternary nitrides in excellent agreement with first-principles DFT calculations, therefore providing solid grounds for using the supercells relaxed using this method as high-quality input for the subsequent local polarization calculation. An extensive article with the details and validity of our method is currently in preparation and will be published elsewhere.

Making use of the expressions derived throughout this chapter, and the VFF just outlined, we have calculated the local polarization for InGaN/GaN QWs with 30% In content in both polar and nonpolar orientations, as shown in Figs. 7(a) and 7(b), respectively. Note that the component shown in the color code is the component of the polarization along the c axis. The corresponding polarization potential is shown in Figs. 7(c), for the polar case, and (d), for the non-polar situation. The polar structure shows a potential profile with the

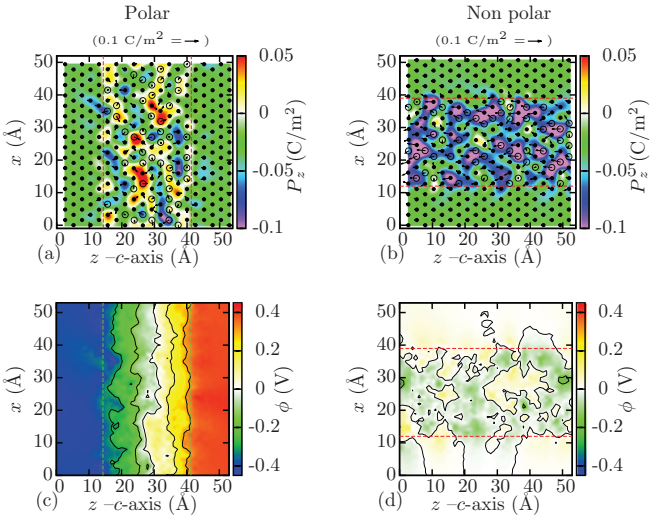

FIG. 7. (Color online) Sections in a plane parallel to the c axis of $In_{0.3}Ga_{0.7}N$/GaN QWs in polar and nonpolar orientations. The component of the polarization along the c axis, P_z, for the polar and nonpolar structures is shown in (a) and (b), respectively. The corresponding polarization potential is shown in (c) and (d). The dashed lines indicate the approximate location of the interfaces between well and barriers. The arrows in (a) and (b) give the direction of the polarization in the xz plane, as well as its magnitude in the same units as the arrow in the legend, which indicates 0.1 C/m^2. Solid circles are Ga atoms and open circles are In atoms.

main features of a capacitorlike structure, although significant fluctuations can also be observed. For a constant value of the polarization, i.e., with no local effects taken into account, the isolines in Fig. 7(c) would be perfectly parallel to each other, as seen already in Fig. 6. In the nonpolar case [see Fig. 7(d)], there are no main features in the potential but only local effects.

Note that the nonpolar QW situation is similar to a bulk calculation in the sense that there are no macroscopic polarization discontinuities, and the polarization potential landscape is only affected by local effects. The importance of these local effects will be highlighted in the next section where we present tight-binding calculations of the electronic structure of bulk InGaN alloys.

V. TIGHT-BINDING MODEL FOR ELECTRONIC STRUCTURE CALCULATION

In this section, we outline the ingredients for our electronic structure calculations. We begin in Sec. V A by introducing the tight-binding (TB) model used to study the band-gap bowing in InGaN alloys. We first introduce the TB model employed to describe the binary bulk materials InN and GaN. We then outline how strain and built-in potential are included in the description as well as how the TB model is implemented to describe the ternary material InGaN.

A. Binary bulk systems

To investigate the band-gap bowing of ternary materials, a microscopic description of the system is required. An ideal solution to this problem would be to perform DFT-based

calculations. However, standard DFT approaches fail to provide an accurate description of the band gaps, especially for systems with a small band gap.[65] As we have seen, standard calculations within LDA or GGA tend to predict a metallic phase for InN, while experiments show a band gap of 0.6–0.7 eV.[37] As we have previously discussed, HSE hybrid functional DFT calculations[43,44] have attracted considerable attention since within this framework one reduces these band-gap problems.[65] Even though standard HSE-DFT calculations circumvent problems with the band gap, in general, these methods still underestimate the band gaps of InN, GaN, and AlN.[65] Especially, if one aims for a comparison with experimentally determined transition energies and band-gap bowing parameters, an accurate description of the band gaps of the binary compounds becomes important. Therefore an approach is required which reproduces effective masses, energetic positions of the different valence bands (VBs) and conduction bands (CBs) and additionally gives band gaps of the binary compounds in agreement with experiment. On the other hand, this approach must also allow for a microscopic description of the alloys. Such a description can be achieved by pseudo-potential[66] or TB calculations.[67] In the following, we apply the TB method to analyze the band-gap bowing in wurtzite InGaN alloys.

More specifically, we use a microscopic sp^3 TB model. In this TB model, the relevant electronic structure of anions and cations is described by the outermost valence orbitals, s, p_x, p_y, and p_z, and the overlap of these basis orbitals is restricted to nearest neighbors. Being only of the order of a few meV, we neglect the spin-orbit (SO) coupling in the model. The inclusion of the SO coupling is straight forward and detailed for example in Ref. 68. However, the crystal field (CF) splitting $\Delta_{\rm cf}$ must be included in the model since it is of significant importance for the accurate description of the VB structure of III-N compounds. Values of $\Delta_{\rm cf}$ lie in the range of 19–24 and 9–38 meV for InN and GaN, respectively, while for AlN $\Delta_{\rm cf} = -230$.[69]

To include the CF splitting in our TB model, we proceed in the following way. As discussed in Ref. 70, the small CF splitting $\Delta_{\rm cf}$ in a WZ crystal differentiates the p_z orbital from the p_x and p_y orbitals. LDA pseudopotential calculations suggest that for the studied materials the bulk CF splitting should be modeled when using the TB method by taking a specific third-nearest-neighbor interactions into account.[71] The TB model we are using here considers only nearest-neighbor hopping matrix elements and treats the four nearest-neighbor atoms as equivalent. To account for the CF splitting within the empirical sp^3 TB model with nearest-neighbor coupling, we introduce the additional parameter $E(p_z,a)$ on the anion sites for the on-site matrix elements of the p_z orbitals. This additional term is used to reproduce the splitting of the valence bands at the zone center (Γ point). Such an approach has also been applied for CdSe QDs with a wurtzite structure.[72] With four atoms per unit cell, the resulting Hamiltonian is a 16×16 matrix for each $\mathbf{k}$ point. This Hamiltonian parametrically depends on the different TB matrix elements, as, for example, shown in Ref. 70.

In general, the TB matrix elements are treated as parameters and are determined by fitting the bulk TB band structure to DFT band structures. In doing so, the TB parameters are designed

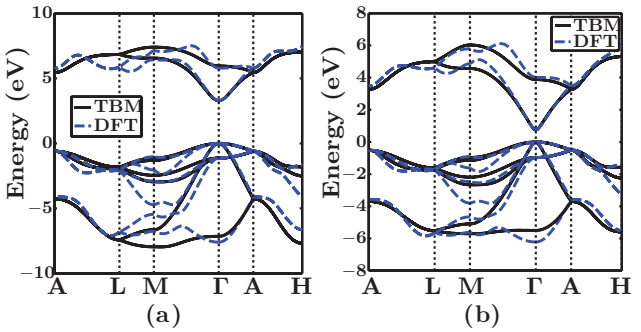

FIG. 8. (Color online) Bulk band structure of wurtzite (a) GaN and (b) InN obtained using HSE-DFT (dashed line) and our sp^3 TB model (solid line).

to reproduce the characteristic features of the DFT band structures, such as energy gaps and splittings between different VBs and CBs. Here, we have performed HSE-DFT band structure calculations for InN and GaN according to the guidelines given in Ref. 47. We used a Γ-centered $6 \times 6 \times 4$ k mesh, and cutoff energy of 600 eV for plane waves. These are the same settings as have been used in Sec. II C1 for the calculation of the polarization-related parameters for the III-N compounds. Recently, we have used the same settings to perform HSE-DFT based calculations for elastic constants in wurtzite InN, AlN, and GaN.[29] These calculations gave elastic constants in very good agreement with available experimental data.[29,73] The HSE-DFT band structure serves as the reference for the TB fitting procedure, for which we use a least-square fitting at the Γ point and $\mathbf{k}$ points along the Γ-A and Γ-M directions, following the guidelines given in Ref. 74. This ensures that the energetic positions near the CB and VB edges as well as the curvature of the different TB bands in the vicinity of the Γ point are in good agreement with the HSE-DFT calculations. Furthermore, using the guidelines of Ref. 74, chemical trends are also taken into account. The resulting TB band structures in comparison with the HSE-DFT band structure for InN and GaN are shown in Fig. 8.

However, as discussed above, and for example in more detail in Ref. 65, even HSE-DFT calculations underestimate the bulk band gap. Since this quantity is of central importance for a detailed comparison with experimental data, we adjust our TB model to reproduce the experimental band gap. In order to do so, here we shift the on-site cation s-orbital energies. This procedure affects mainly the CB edge and bands energetically further away from the VB and CB edges. These bands are of secondary importance for the description of the band-gap bowing in InGaN alloys. Table II summarizes the resulting TB parameters.

B. Tight-binding description for alloys

In the framework of a TB model, the InGaN alloy is modeled on an atomistic level. The TB parameters at each atomic site $\mathbf{R}$ of the underlying wurtzite lattice are first set according to the bulk values of the respective occupying atoms. While for the cation sites (Ga, In) the nearest neighbors are always nitrogen atoms and there is no ambiguity in assigning the TB on-site and nearest neighbor matrix elements, this

TABLE II. Tight-binding parameters (in eV) for the nearest neighbor sp^3 model of wurtzite InN and GaN. The notation of Ref. 70 is used.

	InN	GaN
$E(s,a)$	−11.92	−10.62
$E(p,a)$	0.49	0.82
$E(p_z,a)$	0.46	0.79
$E(s,c)$	0.48	0.91
$E(p,c)$	6.53	6.68
$V(s,s)$	−1.61	−5.97
$V(x,x)$	1.79	2.34
$V(x,y)$	4.83	5.47
$V(sa,pc)$	1.89	4.09
$V(pa,sc)$	6.14	8.67

classification is more difficult for the nitrogen atoms. In this case, the nearest-neighbor environment is a combination of In and Ga atoms. Here, we apply the widely used approach of using weighted averages for the on-site energies according to the number of neighboring In and Ga atoms.[75–77] The hopping matrix elements are chosen according to the values for InN or GaN.

In setting up the Hamiltonian, one must also include the local strain $\epsilon_{ij}(\mathbf{r})$ and the total built-in potential ϕ to ensure an accurate description of the electronic properties of the InGaN alloy. Several authors have shown that this can be done by introducing on-site corrections to the TB matrix elements $H_{l\mathbf{R}',m\mathbf{R}}$,[78,79] where $\mathbf{R}$ and $\mathbf{R}'$ denote lattice sites and l and m are the orbital types. Therefore, we proceed in the following way. The strain dependence of the TB matrix elements is included via the Pikus-Bir Hamiltonian[80,81] as a site-diagonal correction:

$$H^{\mathrm{str}}_{l\mathbf{R},m\mathbf{R}} = \begin{pmatrix} S_s & 0 & 0 & 0 \\ 0 & S_x & S_{xy} & S_{xz} \\ 0 & S_{xy} & S_y & S_{yz} \\ 0 & S_{xz} & S_{yz} & S_z \end{pmatrix}, \tag{22}$$

with

$$\begin{aligned} S_s &= a_{ct}(\epsilon_{11}+\epsilon_{22}) + a_{cp}\epsilon_{zz}, \\ S_x &= (D_2+D_4)(\epsilon_{11}+\epsilon_{22}) + D_5(\epsilon_{11}-\epsilon_{22}) \\ &\quad + (D_1+D_3)\epsilon_{33}, \\ S_y &= (D_2+D_4)(\epsilon_{11}+\epsilon_{22}) - D_5(\epsilon_{11}-\epsilon_{22}) \\ &\quad + (D_1+D_3)\epsilon_{33}, \\ S_z &= D_2(\epsilon_{11}+\epsilon_{11}), \\ S_{xy} &= 2D_5\epsilon_{12}, \\ S_{xz} &= \sqrt{2}D_6\epsilon_{13}, \\ S_{yz} &= \sqrt{2}D_6\epsilon_{23}, \end{aligned} \tag{23}$$

where the D_i denote the VB deformation potentials, while a_{cp} and a_{ct} are the CB deformation potentials.[82] With this approach, the relevant deformation potentials for the highest VB and lowest CB states are included directly without any fitting procedure. In the work described below, the deformation potentials for InN and GaN are taken from HSE-DFT calculations.[47] Again, on the same footing as in the case of the on-site energies for the nitrogen atoms, we use weighted averages to obtain the strain-dependent on-site corrections for $In_xGa_{1-x}N$. Our approach is similar to that used for the strain dependence in an eight-band $\mathbf{k}\cdot\mathbf{p}$ model,[80] but has the benefit that the TB Hamiltonian still takes the correct symmetry of the system into account, and is sensitive to In, Ga, and N atoms.

To obtain the local strain tensor $\epsilon_{ij}(\mathbf{r})$ at each lattice site, we perform in a first step a relaxation of the atomic positions in $In_xGa_{1-x}N$ supercells based on the VFF outlined in Sec. IV. From the relaxed atomic positions, we calculate $\epsilon_{ij}(\mathbf{r})$ according to the method in Ref. 62 via[83]

$$\begin{aligned} \begin{pmatrix} \epsilon_{xx} & \epsilon_{xy} & \epsilon_{xz} \\ \epsilon_{yx} & \epsilon_{yy} & \epsilon_{yz} \\ \epsilon_{zx} & \epsilon_{zy} & \epsilon_{zz} \end{pmatrix} &= \begin{pmatrix} R^0_{12,x} & R^0_{23,x} & R^0_{34,x} \\ R^0_{12,y} & R^0_{23,y} & R^0_{34,y} \\ R^0_{12,z} & R^0_{23,z} & R^0_{34,z} \end{pmatrix}^{-1} \\ &\quad \times \begin{pmatrix} R_{12,x} & R_{23,x} & R_{34,x} \\ R_{12,y} & R_{23,y} & R_{34,y} \\ R_{12,z} & R_{23,z} & R_{34,z} \end{pmatrix} - \mathbb{1}, \end{aligned} \tag{24}$$

where $\mathbf{R}_{12}$, $\mathbf{R}_{23}$, and $\mathbf{R}_{34}$ are the distorted tetrahedron edges, while $\mathbf{R}^0_{12}$, $\mathbf{R}^0_{23}$, and $\mathbf{R}^0_{34}$ are the ideal tetrahedron edges. $\mathbb{1}$ is the 3×3 identity matrix. The built-in potential ϕ is likewise included as a site-diagonal contribution in the TB Hamiltonian. This is also a widely used approach.[84–86]

VI. RESULTS

In the following, we use our TB model, including local strain and built-in potentials to analyze the band-gap bowing of InGaN. We outline the procedure for TB supercell calculations in Sec. VI A, while in Sec. VI B, we compare our theoretical results for transition energies and band-gap bowing parameters against experimental and other theoretical data. The impact of local alloy composition, local strain and local built-in potential on the CB and VB edges of InGaN alloys is discussed in Sec. VI C.

A. TB supercell calculations for InGaN

In the following, all calculations are performed on supercells containing approximately 12 000 atoms, with periodic boundary conditions applied. A large number of atoms are included in the supercell to suppress the influence of finite-size supercell effects. We assume that InGaN is a random alloy, following recent experimental indication.[87,88] For each In concentration, we have performed calculations with five different microscopic configurations, where the In atoms are placed randomly in the supercell. We calculate the band gap $E_g(x)$ as a configurational average, i.e.,

$$E_g(x) = \frac{1}{N}\sum_{i=1}^{N}\left[E^i_{\mathrm{CB}}(x) - E^i_{\mathrm{VB}}(x)\right], \tag{25}$$

where i denotes the microscopic configuration and E^i_{CB} (E^i_{VB}) is the corresponding CB (VB) edge. The number of configurations is given by N.

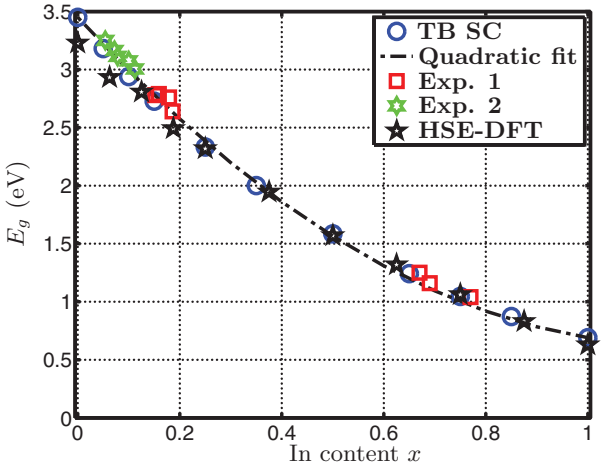

FIG. 9. (Color online) Band gap E_g of $In_xGa_{1-x}N$ as a function of the In content x. Our TB supercell calculations (TB SC) are compared with experimental and theoretical data. The dashed dotted line indicates the quadratic fit, Eq. (26), to the TB data. Experimental data are taken from Sakalauskas *et al.*[91] and Schley *et al.*[90] (Exp. 1) and from McCluskey *et al.*[89] (Exp. 2). Theoretical HSE-DFT data taken from Moses *et al.*[65]

B. Band gap bowing in InGaN: Comparison with experiment

Figure 9 shows TB supercell calculation results (open blue circles) for the band gap E_g of $In_xGa_{1-x}N$ as a function of the In content x. The TB results are compared to recent experimental data[89–91] and HSE-DFT calculations.[65] From Fig. 9, one can infer that our TB results are in excellent agreement with the HSE-DFT results for In contents above 15%–20% ($x > 0.15$–0.2). For values below 15%, the fact that the HSE-DFT calculations underestimate the band gap of GaN becomes important. However, in this composition regime ($x < 0.2$), our TB results are in very good agreement with the experimental data, cf. Fig. 9. Also in the high In content regime ($x > 0.5$), the TB data is in very good agreement with the experimental data. We have applied this model to AlInN too, also showing an excellent agreement with recent experimental data.[92]

For the design of $In_xGa_{1-x}N$ based optoelectronic devices, knowledge about the behavior of the band gap E_g with composition x is of central importance. Usually the dependence of E_g on x is described by a quadratic function in x, involving the energy gaps of InN (E_g^{InN}), GaN (E_g^{GaN}) and a bowing parameter b:

$$E_g = xE_g^{\mathrm{InN}} + (1-x)E_g^{\mathrm{GaN}} - b(1-x)x. \qquad (26)$$

Commonly, the band-gap bowing parameter b of InGaN is assumed to be composition *independent*.[52] We start with this assumption and denote the composition independent bowing parameter by $\tilde{b}$. In doing so we find a bowing parameter $\tilde{b} \approx 2$ eV. Experimentally determined bowing parameters scatter quite significantly, ranging from 1.43 to 2.8 eV. Theoretical values for $\tilde{b}$ range from 1.36 to 5.14 eV. Compared to both theory and experiment our reported value of $\tilde{b} \approx 2$ eV is therefore within the range of the reported literature values. However, it has been suggested[93,94] that the bowing parameter of $In_xGa_{1-x}N$ alloys is composition dependent. Based on HSE-DFT calculations for special quasirandom structures (SQSs), Moses *et al.*[65] found that b ranges in $In_xGa_{1-x}N$ from 2.29 eV ($x = 0.0625$) to 1.14 eV ($x = 0.875$). Gorczyca *et al.*[95] used LDA + C calculations to analyze b in $In_xGa_{1-x}N$ alloys. The authors considered two types of alloys, i.e., (i) alloys with uniformly distributed In atoms in a 32-atom supercell and (ii) alloys with all In atoms clustered. In case (i) Gorczyca *et al.*[95] reported that b ranges from 1.7 eV (large x) to 2.8 eV (small x). For $x = 0.5$, the authors found for the uniform case $b(0.5) = 2.1$ eV. Looking at case (ii), the clustered alloy, band-gap bowing values between 2.5 eV (large x) and 6.5 eV have been reported, with $b(0.5) = 3.9$ eV. Based on our random TB supercell calculations, we find that our bowing parameter shows a strong composition dependence. The TB results for b are summarized in Table III. Here, the values for b range from 1.78 eV (large x) to 2.77 eV (small x). At $x = 0.5$ we find $b = 1.94$ eV. Therefore our results are close to the results obtained from the LDA + C calculations in the case of an uniform alloy (see above).

To shed more light on the composition dependence of b, we investigate in a second step how the CB and VB edge behave as a function of the In content x. These quantities are also of great interest for the design of InGaN/GaN based optoelectronic devices, since the CB and VB edge energies in InGaN affect the confinement energies of electron and hole wave functions. Here, to calculate the bowing parameters $b^{\mathrm{CB}}(x)$ and $b^{\mathrm{VB}}(x)$ for the CB and VB edges, respectively, we use

$$E_{\mathrm{CB}} = \left(E_g^{\mathrm{InN}} + \Delta E_{\mathrm{VB}}\right)x + E_g^{\mathrm{GaN}}(1-x) - b^{\mathrm{CB}}(1-x)x,$$
$$E_{\mathrm{VB}} = \Delta E_{\mathrm{VB}}x - b^{\mathrm{CB}}(1-x)x, \qquad (27)$$

where E_{CB} and E_{VB} are the CB and VB edges, respectively. These quantities are obtained from our TB SC calculations. The VB offset is denoted by ΔE_{VB} and taken from HSE-DFT data in Ref. 65. Here, $b^{\mathrm{CB}}(x)$ and $b^{\mathrm{VB}}(x)$ are composition-dependent fitting parameters to reproduce E_{CB} and E_{VB}, respectively. The resulting composition-dependent values for $b^{\mathrm{CB}}(x)$ and $b^{\mathrm{VB}}(x)$ are summarized in Table III. From this table one infers that, while b^{VB} is almost composition independent, b^{CB} varies significantly with x. Consequently, the composition dependence of the band-gap bowing b arises mainly from the composition dependence of the CB edge. This result is in agreement with the HSE-DFT findings of Ref. 65. Therefore, when modeling InGaN based heterostructures in

TABLE III. Band-gap bowing parameter $b(x)$ of $In_xGa_{1-x}N$ as a function of the In content x.

x	5%	10%	15%	25%	35%	50%	65%	75%	85%
b (eV)	2.77	2.6	2.42	2.28	2.13	1.94	1.82	1.78	1.82
b^{CB} (eV)	1.74	1.56	1.43	1.26	1.13	0.92	0.85	0.81	0.78
b^{VB} (eV)	−1.03	−1.04	−0.99	−1.02	−1.00	−1.02	−0.97	−0.97	−1.04

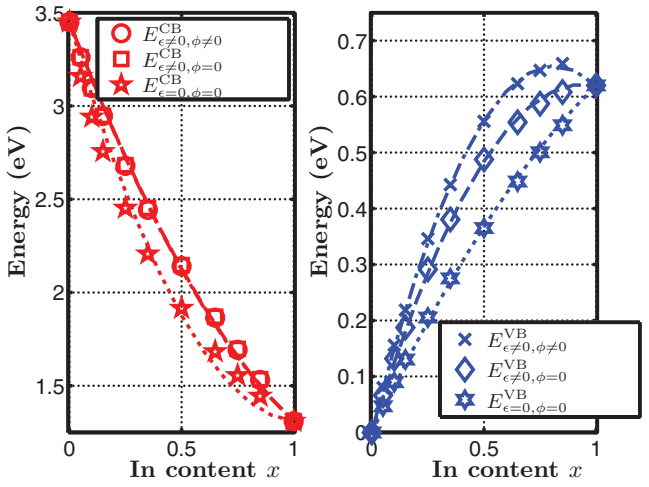

FIG. 10. (Color online) CB (left) and VB (right) edges of $In_xGa_{1-x}N$ as a function of the In content x. Dotted line: fit to data without strain and built-in potential ($VB/CB_{\epsilon=0,\phi=0}$); dashed line: fit to data with strain but without built-in potential ($VB/CB_{\epsilon\neq0,\phi=0}$); dashed-dotted line: fit to data with strain and built-in potential ($VB/CB_{\epsilon\neq0,\phi\neq0}$).

the framework of a continuum description, such as **k**·**p** theory, the composition dependent bowing of the band edges should be taken into account in order to achieve a realistic description of these systems.

To extend the analysis of the band edges in InGaN alloys further, we focus in the next section on the impact of local composition, local strain and local built-in potentials on the CB and VB edges, respectively.

C. Impact of local composition, strain and built-in potential on CB and VB edges in InGaN

In the previous section, we have discussed the composition dependence of the bowing parameters $b^{CB}(x)$ and $b^{VB}(x)$ of the CB and VB edges, respectively. These calculations included local strain and built-in potential effects due to alloy fluctuations. Here, we analyze in more detail how the different contributions from pure alloy fluctuations, local strain and built-in potential effects influence the CB and VB edge energies. Figure 10 shows the CB (left) and VB (right) edge energies as a function of the In content x.

In a first step, to study the impact of the alloy fluctuations only, we neglect the local strain and built-in field effects in the TB SC calculations of the band edges ($E^{CB}_{\epsilon\neq0,\phi\neq0}$, $E^{VB}_{\epsilon\neq0,\phi\neq0}$). As Fig. 10 shows, in the absence of strain and built-in potential, $E^{VB}_{\epsilon=0,\phi=0}$ varies almost linearly with the In content x, while $E^{CB}_{\epsilon=0,\phi=0}$ shows a strong nonlinear behavior. Using Eq. (27), we can determine $\tilde{b}^{CB}$ and $\tilde{b}^{VB}$ for the case of $\epsilon=0,\phi=0$. The results for the composition-independent bowing parameters $\tilde{b}^{CB}$ and $\tilde{b}^{VB}$ are summarized in Table IV. When including local strain effects but neglecting the local built-in potential, $E^{CB}_{\epsilon\neq0,\phi=0}$ is shifted to higher energies over the whole composition range due to hydrostatic strain in the system, (cf. Fig. 10). This reduces the CB edge bowing parameter $\tilde{b}^{CB}$ by a factor of two compared to the situation without strain and built-in potential effects (cf. Table IV).

TABLE IV. Overall band gap ($\tilde{b}^{full}$), CB ($\tilde{b}^{CB}$), and VB $\tilde{b}^{VB}$ bowing parameters. The results are shown in the absence of strain and built-in potential ($\epsilon=0,\phi=0$), in absence of the built-in potential but in the presence of strain ($\epsilon\neq0,\phi=0$), and finally, with strain and built-in potential included ($\epsilon\neq0,\phi\neq0$).

	$\tilde{b}$ (eV)	$\tilde{b}^{CB}$ (eV)	$\tilde{b}^{VB}$ (eV)
$\epsilon=0,\phi=0$	2.24	2.01	−0.23
$\epsilon\neq0,\phi=0$	1.70	1.01	−0.69
$\epsilon\neq0,\phi\neq0$	2.02	1.03	−0.99

When looking at the behavior of $E^{VB}_{\epsilon\neq0,\phi=0}$ in comparison to $E^{VB}_{\epsilon=0,\phi=0}$ we find also a shift to higher energies resulting from biaxial compressive strain. However, in this case, the magnitude of the VB edge bowing parameter $\tilde{b}^{VB}$ is increased by a factor of three compared to the situation without strain and built-in potential (cf. Table IV). When including both local strain and built-in potential effects, $E^{CB}_{\epsilon\neq0,\phi\neq0}$ in comparison to $E^{CB}_{\epsilon\neq0,\phi=0}$ is almost unaffected. This is also reflected in the data for the CB edge bowing parameter $\tilde{b}^{CB}$ shown in Table IV. For the VB edge, this is not the case. Here, the local built-in potential significantly modifies the VB edge, as seen in Fig. 10. Moreover, due to local built-in potential effects, $E^{VB}_{\epsilon\neq0,\phi\neq0}$ exceeds the InN/GaN VB offset ΔE_{VB}. The consequence of this behavior would be that $In_xGa_{1-x}N$ on InN would be a type-II heterostructure for $x \gtrsim 0.6$.

This difference in the behavior of the CB and VB edges can be attributed in part to the differences in the effective masses. Compared to the VB, the effective mass of the CB edge is small.[81,96] Therefore, in the regime of large x (high In content), the randomly distributed In atoms can form QD-like regions that lead to a localization of VB wave functions since the local compressive strain favors this behavior.[97] Therefore we observe a strong increase in the magnitude of $\tilde{b}^{VB}$ when including strain effects, cf. Fig. 10 and Table IV. In contrast, the compressive hydrostatic strain in these regions leads to a weaker localization of the CB wave functions and a shift to higher energies,[97] as observed in Fig. 10. However, since the CB wave functions are only weakly localized in the QD-like regions due to strain effects and the low effective masses, the local built-in potential is of secondary importance for the CB edge. However, originating from the much stronger VB wave function localization, as in a "real" nitride-based QD, the built-in potential further increases the localization and leads to a pronounced shift to higher energies.[12] As seen for example in experiments on c-plane GaN/AlN QDs, due to the presence of the built-in potential the measured photoluminescence (PL) energy drops below the GaN band gap value.[98]

VII. SUMMARY

We have presented a complete theory of local electric polarization in the linear piezoelectric limit. The connection between the local polarization and local internal strain is obtained in an elegant manner through the use of Born effective charges and internal strain parameters. We have validated the theory for the highly ionic III-N wurtzite compounds, demonstrating a high degree of agreement between our model and Berry-phase calculations. We have cast these local effects

in the form of a local piezoelectric tensor, which helps to highlight the importance of local strain and tetrahedron orientation on the polarization field and potential. In addition to this, we have obtained a consistent series of polarization-related *ab initio* parameters for the group-III nitrides.

We have also presented a point dipole method for the calculation of the local polarization potential that overcomes resolution problems encountered when solving directly Poisson's equation. The method involves the discretization of the polarization field as a series of point dipoles. The accuracy of the method has been tested against a well known problem with analytical solution. As an example, we have applied our theory and methodology to study the local polarization and local polarization potential in polar and nonpolar InGaN/GaN QW structures, where we have observed large local fluctuations in both quantities.

Finally, we have presented a tight-binding model that allows us to take into account local alloy effects, including local strain and the local polarization potential discussed throughout the paper. With this model we have calculated the composition dependence of the band gap of InGaN and provided composition-dependent bowing parameters for the band gap and both the conduction- and valence-band edge energies. Furthermore, we have shown that the local polarization potential has a strong influence on wave function localization effects in the valence band of this material.

ACKNOWLEDGMENTS

M. A. C. would like to thank Vincenzo Fiorentini and David Vanderbilt for very useful discussions on the practicalities of Berry-phase calculations. S. S. would like to thank Muhammad Usman for valuable discussions. This work was carried out with the financial support of Science Foundation Ireland under project number 10/IN.1/I2994. S. S. also acknowledges financial support from the European Union Seventh Framework Programme (ALIGHT FP7-280587).

APPENDIX A: EXAMPLE OF THE CALCULATION OF A LOCAL PIEZOELECTRIC COEFFICIENT

To illustrate how the calculation of the local piezoelectric tensor in terms of the internal strain parameters is done, we give here the details of the calculation for $e_{15}^{*,\mathrm{A}}$. The expression of $e_{ij}^{*,X}$ for $e_{15}^{*,\mathrm{A}}$ is simplified to

$$e_{15}^{*,\mathrm{A}} = e_{15}^{(0)} - \frac{e\mathcal{Z}_1^{\mathrm{A}}}{\sqrt{3}{a_0}^2 c_0}\left(\frac{\partial \mu_1^{\mathrm{A}}}{\partial \epsilon_5} - \frac{1}{2}\mu_{3,0}^{\mathrm{A}}\right), \tag{A1}$$

where we have made use of the Voigt relation $\partial\epsilon_{13}/\partial\epsilon_5 = 1/2$. $\mu_{3,0}^{\mathrm{A}} = 4(u_0 - 3/8)c_0$ is given by the WZ internal parameter, and $\mathcal{Z}_1^{\mathrm{A}} \equiv \mathcal{Z}_1$ for A being a cation. We need to calculate μ_1^{A}. Looking at Fig. 3, it is clear that the nearest neighbors of A are B, which we label 1, and three periodic replicas of D contained in a plane below A, which we label 2–4. If A is fixed at the origin, $\mathbf{r}_{\mathrm{A}} = (0,0,0)$, then the distances of the different nearest neighbors from A are given by

$$\begin{aligned} \boldsymbol{\ell}^1 &= \mathbf{r}_{\mathrm{B}}, \quad \boldsymbol{\ell}^2 = \mathbf{r}_{\mathrm{D}} - \mathbf{c}, \\ \boldsymbol{\ell}^3 &= \mathbf{r}_{\mathrm{D}} - \mathbf{c} - \mathbf{a}, \quad \boldsymbol{\ell}^4 = \mathbf{r}_{\mathrm{D}} - \mathbf{c} - \mathbf{b}, \end{aligned} \tag{A2}$$

where **a**, **b**, and **c** are the (strained) lattice vectors of the unit cell. Since for this example we are interested in $e_{15}^{*,\mathrm{A}}$ only, we set all the strain components to zero except for $\epsilon_5 = 2\epsilon_{13}$. Following all the definitions given in Ref. 29 (with exchanged notation $\epsilon_{13} \leftrightarrow \epsilon_{xz}$), we can write

$$\begin{aligned} \mathbf{r}_{\mathrm{B}} &= [u_0 c_0 \epsilon_{13}, 0, u_0 c_0] + [\zeta_1 c_0 \epsilon_{13}, 0, 0], \\ \mathbf{r}_{\mathrm{D}} &= \left[\frac{a_0}{2} + \left(\frac{1}{2} + u_0\right) c_0 \epsilon_{13}, \frac{\sqrt{3}a_0}{6}, \left(\frac{1}{2} + u_0\right) c_0 + \frac{a_0}{2}\epsilon_{13}\right] \\ &\quad + [\zeta_1 c_0 \epsilon_{13}, 0, 0], \\ \mathbf{a} &= [a_0, 0, a_0 \epsilon_{13}], \quad \mathbf{b} = \left[\frac{a_0}{2}, \frac{\sqrt{3}a_0}{2}, \frac{a_0}{2}\epsilon_{13}\right], \\ \mathbf{c} &= [c_0 \epsilon_{13}, 0, c_0]. \end{aligned} \tag{A3}$$

To obtain μ_1^{A} we sum over nearest-neighbor distances:

$$\mu_1^{\mathrm{A}} = \sum_{\alpha=1}^{4} \ell_1^{\alpha} = 4u_0 c_0 \epsilon_{13} - \frac{3}{2} c_0 \epsilon_{13} + 4\zeta_1 c_0 \epsilon_{13}. \tag{A4}$$

The last term of Eq. (A1) therefore reduces to

$$\begin{aligned} \frac{\partial \mu_1^{\mathrm{A}}}{\partial \epsilon_5} - \frac{1}{2}\mu_{3,0}^{\mathrm{A}} &= 2\left(u_0 - \frac{3}{8}\right) c_0 + 2\zeta_1 c_0 - 2\left(u_0 - \frac{3}{8}\right) c_0 \\ &= 2\zeta_1 c_0, \end{aligned} \tag{A5}$$

which leads to the final result:

$$e_{15}^{*,\mathrm{A}} = e_{15}^{(0)} - \frac{2e\mathcal{Z}_1}{\sqrt{3}{a_0}^2}\zeta_1. \tag{A6}$$

APPENDIX B: POINT DIPOLE METHOD FOR THE CALCULATION OF LOCAL POLARIZATION POTENTIALS

Proceeding in a similar manner to the one employed by Jackson for a point charge,[59] we can obtain the exact analytic solution for the potential due to a point dipole when only one

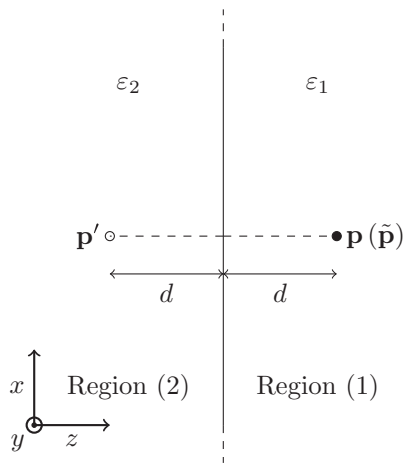

FIG. 11. Schematic representation of the two media with different dielectric constant and point dipole **p** problem. The image dipoles **p**′ and $\tilde{\mathbf{p}}$ are needed in order to solve it.

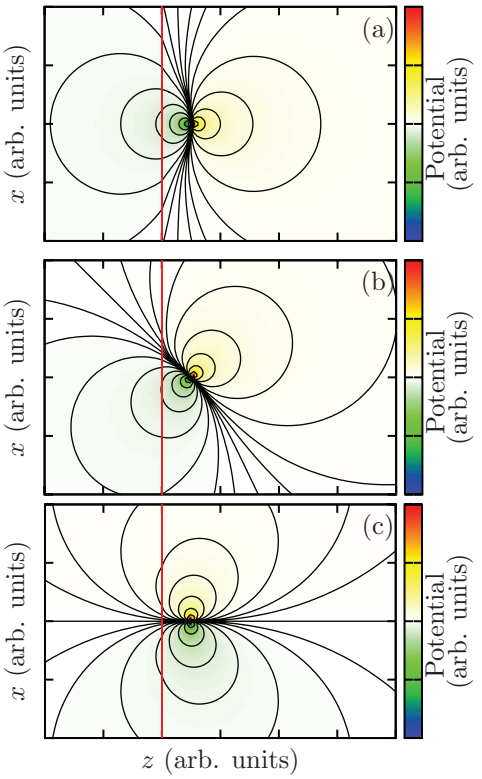

FIG. 12. (Color online) Potential profiles for three dipole orientations in the case of only one planar interface (indicated by the vertical line) and two different dielectric constants. The potential isolines are chosen so they decay exponentially.

interface is present, as schematically shown in Fig. 11:

$$\phi_{\mathbf{p}}^{(1)}(\mathbf{r}) = \frac{1}{4\pi\varepsilon_0\varepsilon_1}\frac{\mathbf{p}\cdot(\mathbf{r}-\mathbf{r}_{\mathbf{p}})}{|\mathbf{r}-\mathbf{r}_{\mathbf{p}}|^3} + \frac{1}{4\pi\varepsilon_0\varepsilon_1}\frac{\mathbf{p}'\cdot(\mathbf{r}-\mathbf{r}_{\mathbf{p}'})}{|\mathbf{r}-\mathbf{r}_{\mathbf{p}'}|^3},$$
$$\phi_{\mathbf{p}}^{(2)}(\mathbf{r}) = \frac{1}{4\pi\varepsilon_0\varepsilon_2}\frac{\tilde{\mathbf{p}}\cdot(\mathbf{r}-\mathbf{r}_{\tilde{\mathbf{p}}})}{|\mathbf{r}-\mathbf{r}_{\tilde{\mathbf{p}}}|^3}, \qquad \text{(B1)}$$

with

$$\mathbf{p}' = \frac{\varepsilon_1-\varepsilon_2}{\varepsilon_1+\varepsilon_2}[p_x,p_y,-p_z], \quad \mathbf{r}_{\mathbf{p}'} = [x_{\mathbf{p}},y_{\mathbf{p}},z_{\mathbf{p}}-2d],$$
$$\tilde{\mathbf{p}} = \frac{2\varepsilon_2}{\varepsilon_1+\varepsilon_2}[p_x,p_y,p_z], \quad \mathbf{r}_{\tilde{\mathbf{p}}} = \mathbf{r}_{\mathbf{p}}, \qquad \text{(B2)}$$

where $\mathbf{p}'$ is the image dipole used, together with the original dipole $\mathbf{p}$, for the calculation of the potential $\phi_{\mathbf{p}}^{(1)}(\mathbf{r})$ in region (1) and $\tilde{\mathbf{p}}$ is the image dipole used for the calculation of the potential $\phi_{\mathbf{p}}^{(2)}(\mathbf{r})$ in region (2). Their positions are given by $\mathbf{r}_{\mathbf{p}'}$ and $\mathbf{r}_{\tilde{\mathbf{p}}}$, respectively. The results for a test dipole of arbitrary magnitude when one of the materials has a dielectric constant twice as big as that of the material in which the dipole is contained are shown in Figs. 12(a)–12(c) for three different orientations of the dipole.

The calculation of the potential when a second interface is included is more complicated, as additional mirror images have to be added to balance the two initial image dipoles about each interface. As a result, an infinite number of reflections (and hence, image dipoles) have to be considered in order to obtain the exact form of the potential. These reflections up to third order are shown in Fig. 13. The treatment for a point charge in such a situation has been already done by Barrera.[99] For the case of a point dipole, we find the expressions to be similar although the transformation of the point dipole is somehow different compared to the point charge due to the vector nature of the former. Details of our treatment and expressions for the three-media case are given in the next section.

1. Point dipole solution for the three-dielectric problem

Building on the description made by Barrera for point charges in a three-dielectric configuration,[99] we give here the analogous solution for point dipoles. The reflections necessary to construct the image point dipoles are illustrated in Fig. 13. Following the convention of Fig. 13, where d is the distance from the dipole to the left side interface and h is the distance

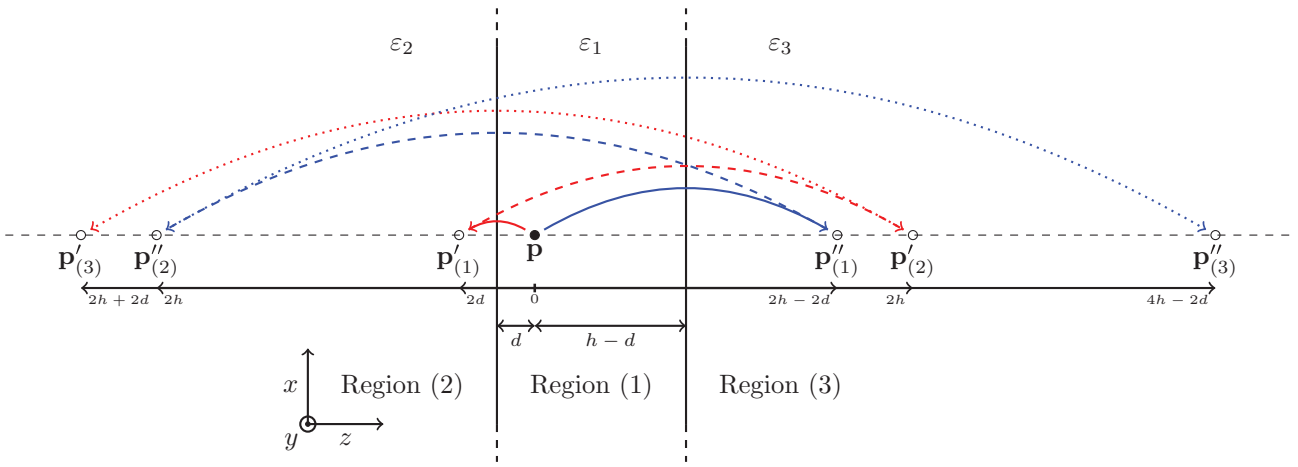

FIG. 13. (Color online) Reflection of image dipoles up to third order in a three-dielectric setup. Each of the reflection sequences is denoted by a different color: the sequence starting to the left and originating the series $\mathbf{p}'_{(n)}$ is coloured in red, whereas the sequence starting to the right and originating the series $\mathbf{p}''_{(n)}$ is in blue. Solid lines indicate first-order reflections, dashed lines indicate second-order reflections and dotted lines indicate third order reflections.

between the two interfaces, we can obtain a set of rules for the form of the image charges $\mathbf{p}'_{(n)}$ and $\mathbf{p}''_{(n)}$, being the nth reflections of $\mathbf{p}$ starting at left and right, respectively. These rules can be written as the following expressions. For the position of the image dipoles:

$$\begin{aligned} z_{\mathbf{p}'_{(2n-1)}} &= z_{\mathbf{p}} - [n\,2d + (n-1)(2h-2d)], \\ z_{\mathbf{p}'_{(2n)}} &= z_{\mathbf{p}} + [n\,2d + n(2h-2d)], \\ z_{\mathbf{p}''_{(2n-1)}} &= z_{\mathbf{p}} + [n(2h-2d) + (n-1)2d], \\ z_{\mathbf{p}''_{(2n)}} &= z_{\mathbf{p}} - [n(2h-2d) + n2d], \end{aligned} \tag{B3}$$

and for the value of the image dipoles:

$$\begin{aligned} \mathbf{p}'_{(2n-1)} &= [p_x, p_y, -p_z]\left(\frac{\varepsilon_1-\varepsilon_2}{\varepsilon_1+\varepsilon_2}\right)^n\left(\frac{\varepsilon_1-\varepsilon_3}{\varepsilon_1+\varepsilon_3}\right)^{n-1}, \\ \mathbf{p}'_{(2n)} &= [p_x, p_y, p_z]\left(\frac{\varepsilon_1-\varepsilon_2}{\varepsilon_1+\varepsilon_2}\right)^n\left(\frac{\varepsilon_1-\varepsilon_3}{\varepsilon_1+\varepsilon_3}\right)^{n}, \end{aligned} \tag{B4}$$

for the first series and

$$\begin{aligned} \mathbf{p}''_{(2n-1)} &= [p_x, p_y, -p_z]\left(\frac{\varepsilon_1-\varepsilon_2}{\varepsilon_1+\varepsilon_2}\right)^{n-1}\left(\frac{\varepsilon_1-\varepsilon_3}{\varepsilon_1+\varepsilon_3}\right)^{n}, \\ \mathbf{p}''_{(2n)} &= \mathbf{p}'_{(2n)}, \end{aligned} \tag{B5}$$

for the second series, with $n \in \mathbb{N}$. Finally, the expression of the potential in all three regions can be written as

$$\begin{aligned} \phi^{(1)}_{\mathbf{p}}(\mathbf{r}) &= \frac{1}{4\pi\varepsilon_0\varepsilon_1}\left\{\frac{\mathbf{p}\cdot(\mathbf{r}-\mathbf{r}_{\mathbf{p}})}{|\mathbf{r}-\mathbf{r}_{\mathbf{p}}|^3} + \sum_{n=1}^{\infty}\left[\frac{\mathbf{p}'_{(n)}\cdot\left(\mathbf{r}-\mathbf{r}_{\mathbf{p}'_{(n)}}\right)}{\left|\mathbf{r}-\mathbf{r}_{\mathbf{p}'_{(n)}}\right|^3} + \frac{\mathbf{p}''_{(n)}\cdot\left(\mathbf{r}-\mathbf{r}_{\mathbf{p}''_{(n)}}\right)}{\left|\mathbf{r}-\mathbf{r}_{\mathbf{p}''_{(n)}}\right|^3}\right]\right\}, \\ \phi^{(2)}_{\mathbf{p}}(\mathbf{r}) &= \frac{1}{4\pi\varepsilon_0\varepsilon_2}\left\{\frac{\mathbf{p}\cdot(\mathbf{r}-\mathbf{r}_{\mathbf{p}})}{|\mathbf{r}-\mathbf{r}_{\mathbf{p}}|^3} + \sum_{n=1}^{\infty}\left[\frac{\mathbf{p}'_{(2n)}\cdot\left(\mathbf{r}-\mathbf{r}_{\mathbf{p}'_{(2n)}}\right)}{\left|\mathbf{r}-\mathbf{r}_{\mathbf{p}'_{(2n)}}\right|^3} + \frac{\mathbf{p}''_{(2n-1)}\cdot\left(\mathbf{r}-\mathbf{r}_{\mathbf{p}''_{(2n-1)}}\right)}{\left|\mathbf{r}-\mathbf{r}_{\mathbf{p}''_{(2n-1)}}\right|^3}\right]\right\}\frac{2\varepsilon_2}{\varepsilon_1+\varepsilon_2}, \\ \phi^{(3)}_{\mathbf{p}}(\mathbf{r}) &= \frac{1}{4\pi\varepsilon_0\varepsilon_3}\left\{\frac{\mathbf{p}\cdot(\mathbf{r}-\mathbf{r}_{\mathbf{p}})}{|\mathbf{r}-\mathbf{r}_{\mathbf{p}}|^3} + \sum_{n=1}^{\infty}\left[\frac{\mathbf{p}'_{(2n-1)}\cdot\left(\mathbf{r}-\mathbf{r}_{\mathbf{p}'_{(2n-1)}}\right)}{\left|\mathbf{r}-\mathbf{r}_{\mathbf{p}'_{(2n-1)}}\right|^3} + \frac{\mathbf{p}''_{(2n)}\cdot\left(\mathbf{r}-\mathbf{r}_{\mathbf{p}''_{(2n)}}\right)}{\left|\mathbf{r}-\mathbf{r}_{\mathbf{p}''_{(2n)}}\right|^3}\right]\right\}\frac{2\varepsilon_3}{\varepsilon_1+\varepsilon_3}. \end{aligned} \tag{B6}$$

It is implicit in Eq. (B6) that for the calculation of the potential $\phi^{(2)}_{\mathbf{p}}$ in region (2) only the image dipoles in region (3) (together with the original dipole) are taken into account, and vice versa. Given the form of Eq. (B6) it is clear that an exact solution to the problem of three media cannot be obtained for a finite number of terms in the summation. However, approximate solutions can be obtained whose accuracy will depend mostly on the difference in the values of the dielectric constants of the different materials. In Fig. 14, we show approximations up to third order reflections, for different orientations of the dipole, in the case of three materials for which $\varepsilon_2 = 2\varepsilon_1$ and $\varepsilon_3 = 3\varepsilon_1$. This is an extreme case in the context of III-V compounds, for which the differences in ε_r between materials do not usually go beyond 50%. For clarity of interpretation, the potential isolines shown decay as a power of 2, which allows to visualize the fine effects of the interfaces far from the dipole. As can be seen, the second order correction [see Figs. 14(d)–14(f)] is already very well converged for this extreme case and we expect first-order corrections to be sufficient for the materials of interest, group-III nitrides, in particular.

2. Gaussian smearing of point dipoles

As mentioned in the paper, the potential solution for a point dipole is an approximation to the potential due to the dipole moment of a charge distribution.[59] This approximation is only valid in the limit when the potential is calculated sufficiently far away from the charge distribution. How far is "sufficiently far" depends on the particular problem at hand, basically on the value of the dipole and the volume over which the charge density giving rise to the dipole moment spread originally. A Gaussian smearing of the dipoles that are close to the position where the potential is calculated, is a straightforward manner to deal with this problem, as the parameters controlling the smearing can be tuned easily at need. We propose the implementation of this smearing controlled by two parameters: (1) r_{smear} is the cutoff radius for which all the dipoles that obey $|\mathbf{r}-\mathbf{r}_{\mathbf{p}}| < r_{\text{smear}}$ are smeared, where $\mathbf{r}$ is the position where the potential is calculated and $\mathbf{r}_{\mathbf{p}}$ is the position of the dipole under consideration. (2) σ is the standard deviation of the Gaussian function that produces the smearing. It gives a measure of the volume over which the dipole is smeared. Therefore the expression for the potential $\phi_{\mathbf{p}}(\mathbf{r})$ at $\mathbf{r}$ due to a dipole $\mathbf{p}$ located at $\mathbf{r}_{\mathbf{p}}$ can be rewritten, in spherical coordinates, as

$$\phi_{\mathbf{p}}(\mathbf{r}) = \begin{cases} \frac{1}{4\pi\varepsilon_0\varepsilon_r}\frac{\mathbf{p}\cdot(\mathbf{r}-\mathbf{r}_{\mathbf{p}})}{|\mathbf{r}-\mathbf{r}_{\mathbf{p}}|^3}, & \text{for} \quad |\mathbf{r}-\mathbf{r}_{\mathbf{p}}| \geqslant r_{\text{smear}}, \\ \frac{1}{4\pi\varepsilon_0\varepsilon_r}\frac{1}{(2\pi\sigma^2)^{\frac{3}{2}}}\int_0^{2\pi}d\varphi\int_0^{\pi}d\theta\int_0^{\infty}d\rho\,\sin\theta\rho^2 e^{-\frac{|\mathbf{r}-\mathbf{r}'_{\mathbf{p}}|^2}{2\sigma^2}}\frac{\mathbf{p}\cdot(\mathbf{r}-\mathbf{r}'_{\mathbf{p}})}{|\mathbf{r}-\mathbf{r}'_{\mathbf{p}}|^3}, & \text{for} \quad |\mathbf{r}-\mathbf{r}_{\mathbf{p}}| < r_{\text{smear}}, \end{cases} \tag{B7}$$

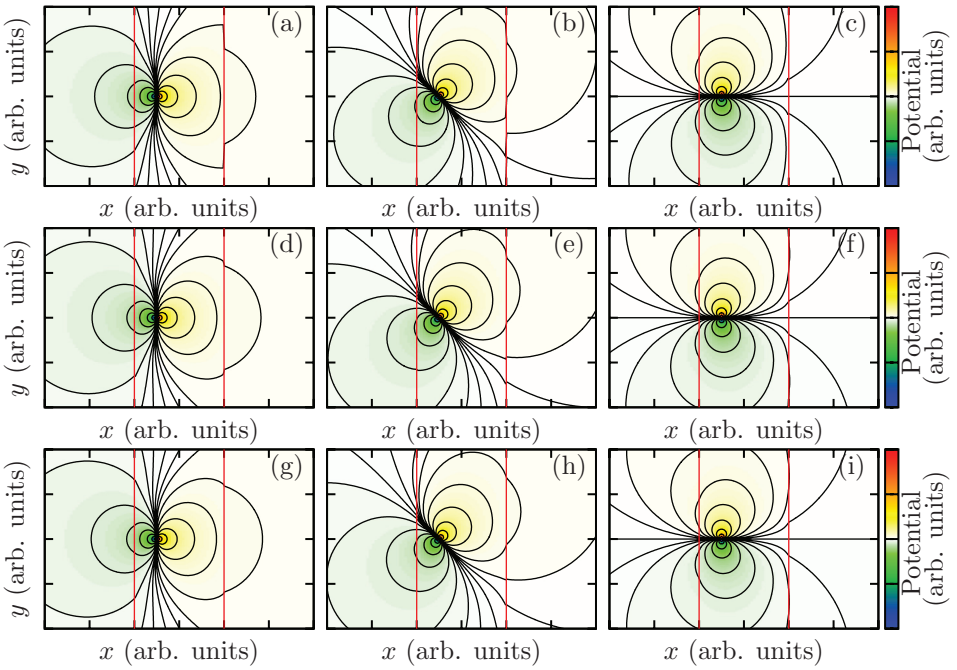

FIG. 14. (Color online) Different approximations for the three media problem shown schematically in Fig. 13 for different orientations of the dipole. (a)–(c) include up to first-order reflections, (d)–(f) second-order reflections, and (g)–(i) include up to third-order reflections. The red lines indicate the interfaces between different materials: the central material has an (arbitrary) permittivity of $\varepsilon = 1$, the material on the left has $\varepsilon = 2$ and the material on the right has $\varepsilon = 3$. It can be seen that third-order reflections are sufficient to converge the potential for that particular set of relative values of ε.

where $\mathbf{r}'_{\mathbf{p}}$ is given by

$$\mathbf{r}'_{\mathbf{p}} = \mathbf{r}_{\mathbf{p}} + [\rho \sin\theta \cos\varphi, \rho \sin\theta \sin\varphi, \rho \cos\theta]. \quad \text{(B8)}$$

Typically, the integration in ρ can be done up to a certain cutoff since the value of the integrand will decay rapidly. For example, our current implementation sets 3.4σ as the upper limit for the integration, which comprises a volume that contains about 99% of the total original dipole moment $\mathbf{p}$. The extension of Eq. (B7) to the case in which different dielectric constants are present is straightforward and done in the same way as explained in the paper and Sec. B 1 of this Appendix.

3. Computational aspects: method of layers and application to quantum wells

It is clear that when dealing with real-size structures, for which the polarization is sampled at a very elevated number of sites, the calculation of the potential $\phi(\mathbf{r})$ becomes very expensive. In particular, for each $\mathbf{r}$, a summation over *all* the dipoles present in the system has to be carried out:

$$\phi(\mathbf{r}) = \sum_{\mathbf{p}} \phi_{\mathbf{p}}(\mathbf{r}). \quad \text{(B9)}$$

In a system where the density of dipoles $n_{\mathbf{p}}$ is approximately constant, for instance one dipole located at each cation site in Ref. 4, the number of dipoles $\delta N_{\mathbf{p}}$ contributing to Eq. (B9) located at distances between R and $R + \delta R$ from $\mathbf{r}$ is proportional to the surface area of a sphere of radius R:

$$\delta N_{\mathbf{p}} \propto 4\pi R^2 n_{\mathbf{p}} \delta R, \quad \text{(B10)}$$

where δR is an infinitesimal increment in R. Because the contribution to $\phi(\mathbf{r})$ from each dipole decreases like $1/R^2$, as given by Eq. (20), Eq. (B10) implies that the contribution to $\phi(\mathbf{r})$ due to the dipoles located at $\mathbf{r}_{\mathbf{p}}$ for which $R < |\mathbf{r} - \mathbf{r}_{\mathbf{p}}| < R + \delta R$ is of the same order of magnitude as the contribution due to dipoles for which $R' < |\mathbf{r} - \mathbf{r}_{\mathbf{p}}| < R' + \delta R$, for any arbitrary $R' > R$. In other words, in principle, the sum in Eq. (B9) does not converge. In practice, for real structures such as InGaN/GaN QWs, the fact that there is a dot product involved in the calculation of the potential due to each dipole, and also that the dipoles in the barrier typically point in the same direction, give rise to opposite contributions that tend to cancel each other as R increases, as schematically shown in Fig. 15. In that case, the sum does converge although rather

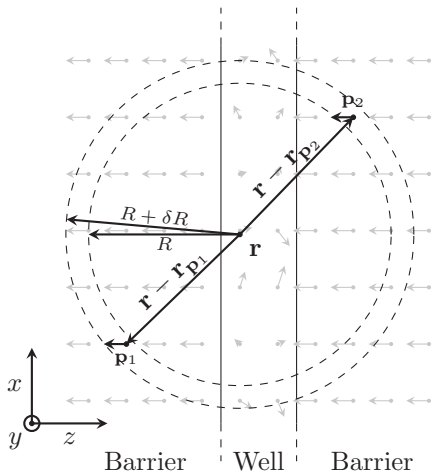

FIG. 15. Schematic representation of the dipoles present in a typical nitride QW structure. In a sphere of radius R from $\mathbf{r}$ there exist a certain number of dipole pairs for which $\mathbf{p}_1 \cdot (\mathbf{r} - \mathbf{r}_{\mathbf{p}_1}) = -\mathbf{p}_2 \cdot (\mathbf{r} - \mathbf{r}_{\mathbf{p}_2})$ and therefore tend to neutralize each other (they do not exactly cancel each other due to the image dipole effect that depends on how far $\mathbf{r}$ and $\mathbf{r}_{\mathbf{p}}$ are from *each* interface). For large R, this cancellation effect is bigger as the polarization is usually constant in the barrier.

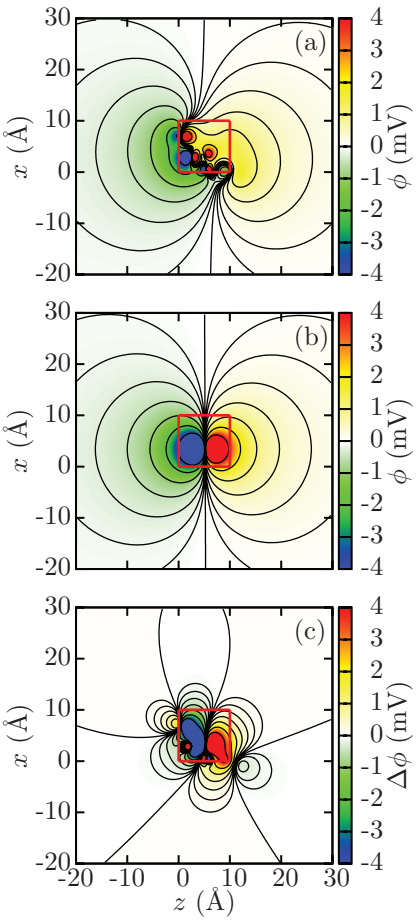

FIG. 16. (Color online) Section in the xz plane of (a) the polarization potential due to an ensemble of 10 dipoles randomly placed inside a cube of side 10 Å with origin at (0,0,0). The boundaries of the cube within the xz plane is indicated by the red line. The dipoles components are given by a Gaussian probability distribution with p_x centered at 10^{-31} Cm, p_y and p_z centered at zero, and standard deviation 5×10^{-32} Cm for all three components; (b) the polarization potential due to a single dipole obtained from the ensemble in (a) calculated by means of Eq. (B11); and (c) difference between the potentials shown in (b) and (a). Note that the potential isolines shown follow an exponential behavior to exaggerate the results: the lines escaping the plots correspond to zero and the outer lobe-shaped isolines indicate ∼6 μV.

slowly. We have implemented two different methods to speed up the convergence of the sum in Eq. (B9), one of which can be applied to any system, the "method of layers." The other method can be applied to systems where some assumption can be made about the value of the polarization being constant in the greatest part of the system, as is the case in QWs. An outline of these methods is given next.

a. Method of layers

In the same way that a point dipole is an approximation for a charge density distribution valid far away from the location of the dipole, it can be shown that a point dipole can be a valid approximation for a given *ensemble* of neighboring point dipoles at a certain distance from the ensemble. Figure 16(a) shows the potential due to an ensemble of N dipoles $\mathbf{p}_i$, of typical magnitude in nitride QWs, that are localized in a restricted region in space, each at position $\mathbf{r}_{\mathbf{p}_i}$. This ensemble can be approximated by a single dipole $\mathbf{P}$ whose magnitude equals the summation of all the original dipoles and whose position $\mathbf{r}_\mathbf{P}$ is given by the weighted average of the dipoles in the ensemble [see Fig. 16(b)]:

$$\mathbf{P} = \sum_{i=1}^{N} \mathbf{p}_i, \quad \mathbf{r}_\mathbf{P} = \frac{1}{|\mathbf{P}|} \sum_{i=1}^{N} \mathbf{r}_{\mathbf{p}_i} |\mathbf{p}_i|. \tag{B11}$$

As shown in Fig. 16(c), the difference between an ensemble of dipoles and its correspondent approximation calculated as in Eq. (B11) decays rapidly away from the ensemble. Applying Eq. (B11) recurrently, one can construct, around the point $\mathbf{r}$ where the potential ϕ is being calculated, a system of "layers" in which the density of dipoles decreases as one moves away from $\mathbf{r}$.

b. Simplification for quantum wells

A simplification can be made for QW systems, or even a quantum dot (QD) system, if a constant value for the polarization can be assumed for the greatest part of the system. Since only *differences* in polarization are meaningful for the calculation of polarization potentials, an arbitrary constant shift of the polarization of the *whole* system will not have any effect on the calculated value of the polarization potential. This shift can be chosen in such a way that the resultant polarization, at least on average, is zero in the barrier in the case of a QW, or in the *unstrained* barrier in the case of a QD.[62,100] In that case, all the dipoles arising from that region, once the discretization described in the main paper is made, will have value zero. Therefore the dipoles contained within that region can be left out of the calculation.

*mcaroba@gmail.com

[1]O. Ambacher, J. Majewski, C. Miskys, A. Link, M. Hermann, M. Eickhoff, M. Stutzmann, F. Bernardini, V. Fiorentini, V. Tilak, B. Schaff, and L. F. Eastman, J. Phys.: Condens. Matter **14**, 3399 (2002).

[2]G. Bester, X. Wu, D. Vanderbilt, and A. Zunger, Phys. Rev. Lett. **96**, 187602 (2006).

[3]A. Beya-Wakata, P.-Y. Prodhomme, and G. Bester, Phys. Rev. B **84**, 195207 (2011).

[4]M. A. Caro, S. Schulz, and E. P. O'Reilly, Phys. Stat. Sol. B **249**, 526 (2012).

[5]M. Grundmann, O. Stier, and D. Bimberg, Phys. Rev. B **52**, 11969 (1995).

[6]S. Schulz, M. A. Caro, E. P. O'Reilly, and O. Marquardt, Phys. Rev. B **84**, 125312 (2011).

[7]T. Takeuchi, S. Sota, M. Katsuragawa, M. Komori, H. Takeuchi, H. Amano, and I. Akasaki, Jpn. J. Appl. Phys. **36**, L382 (1997).

[8]M.-H. Kim, M. F. Schubert, Q. Dai, J. K. Kim, E. F. Schubert, J. Piprek, and Y. Park, Appl. Phys. Lett. **91**, 183507 (2007).

[9]W. Lee, M.-H. Kim, D. Zhu, A. N. Noemaun, J. K. Kim, and E. F. Schubert, J. Appl. Phys. **107**, 063102 (2010).

[10]M. A. Caro, S. Schulz, S. B. Healy, and E. P. O'Reilly, J. Appl. Phys. **109**, 084110 (2011).

[11]S. Schulz and E. P. O'Reilly, Phys. Rev. B **82**, 033411 (2010).

[12]D. P. Williams, S. Schulz, A. D. Andreev, and E. P. O'Reilly, IEEE J. Sel. Top. Quantum Electron. **15**, 1092 (2009).

[13]J. P. Perdew and M. Levy, Phys. Rev. Lett. **51**, 1884 (1983).

[14]A. Seidl, A. Görling, P. Vogl, J. A. Majewski, and M. Levy, Phys. Rev. B **53**, 3764 (1996).

[15]G. Klimeck, S. S. Ahmed, H. Bae, N. Kharche, S. Clark, B. Haley, S. Lee, M. Naumov, H. Ryu, F. Saied, M. Prada, M. Korkusinski, T. B. Boykin, and R. Rahman, IEEE Trans. Electron. Dev. **54**, 2079 (2007).

[16]G. Klimeck, S. S. Ahmed, N. Kharche, M. Korkusinski, M. Usman, M. Prada, and T. B. Boykin, IEEE Trans. Electron. Dev. **54**, 2090 (2007).

[17]J. F. Nye, *Physical Properties of Crystals: Their Representation by Tensors and Matrices* (Oxford University Press, Oxford, 1985).

[18]432 is the Hermann-Mauguin symbol; using the Schoenflies system, the equivalent point group is O (orthorhombic symmetry). While point group 432 does not present *linear* piezoelectricity, Grimmer has shown that it is compatible with second-order piezoelectricity. See H. Grimmer, Acta Crystallogr. Sect. A: Found. Crystallogr. **63**, 441 (2007).

[19]One can also define a second-order piezoelectric tensor to characterize piezoelectricity further away from equilibrium, see Ref. 18.

[20]Note that in Voigt notation, $\epsilon_1 = \epsilon_{xx}, \epsilon_2 = \epsilon_{yy}, \epsilon_3 = \epsilon_{zz}, \epsilon_4 = 2\epsilon_{yz}$, $\epsilon_5 = 2\epsilon_{xz}$ and $\epsilon_6 = 2\epsilon_{xy}$.

[21]R. Resta and D. Vanderbilt, *Physics of Ferroelectrics: a Modern Perspective* (Springer-Verlag, Berlin, Heidelberg, 2007), Chap. Theory of Polarization: A Modern Approach.

[22]R. D. King-Smith and D. Vanderbilt, Phys. Rev. B **47**, 1651 (1993).

[23]D. Vanderbilt and R. D. King-Smith, Phys. Rev. B **48**, 4442 (1993).

[24]R. Resta, Ferroelectrics **136**, 51 (1992).

[25]R. Resta, Rev. Mod. Phys. **66**, 899 (1994).

[26]F. Bernardini, V. Fiorentini, and D. Vanderbilt, Phys. Rev. B **56**, R10024 (1997).

[27]M. A. Caro, S. Schulz, and E. P. O'Reilly, J. Phys.: Condens. Matter **25**, 025803 (2013).

[28]X. Gonze and C. Lee, Phys. Rev. B **55**, 10355 (1997).

[29]M. A. Caro, S. Schulz, and E. P. O'Reilly, Phys. Rev. B **86**, 014117 (2012).

[30]F. Bernardini and V. Fiorentini, Phys. Rev. B **64**, 085207 (2001).

[31]J. Pal, G. Tse, V. Haxha, M. A. Migliorato, and S. Tomić, Phys. Rev. B **84**, 085211 (2011).

[32]V. Fiorentini, F. Bernardini, and O. Ambacher, Appl. Phys. Lett. **80**, 1204 (2002).

[33]P.-Y. Prodhomme, A. Beya-Wakata, and G. Bester, Phys. Rev. B **88**, 121304 (2013).

[34]S. Nakamura, S. J. Pearton, and G. Fasol, *The Blue Laser Diode: the Complete Story* (Springer-Verlag, Berlin, Heidelberg, 2000).

[35]M. R. Krames, O. B. Shchekin, R. Mueller-Mach, G. O. Mueller, L. Zhou, G. Harbers, and M. G. Craford, J. Disp. Technol. **3**, 160 (2007).

[36]U. K. Mishra, L. Shen, T. E. Kazior, and W. Yi-Feng, Proc. IEEE **96**, 287 (2008).

[37]J. Wu, J. Appl. Phys. **106**, 011101 (2009).

[38]T. Aschenbrenner, H. Dartsch, C. Kruse, M. Anastasescu, M. Stoica, M. Gartner, A. Pretorius, A. Rosenauer, T. Wagner, and D. Hommel, J. Appl. Phys. **108**, 063533 (2010).

[39]Vienna *ab initio* simulation package (VASP), http://www.vasp.at, see also on line documentation.

[40]G. Kresse and J. Furthmüller, Phys. Rev. B **54**, 11169 (1996).

[41]P. E. Blöchl, Phys. Rev. B **50**, 17953 (1994).

[42]G. Kresse and D. Joubert, Phys. Rev. B **59**, 1758 (1999).

[43]J. Heyd, G. E. Scuseria, and M. Ernzerhof, J. Chem. Phys. **118**, 8207 (2003).

[44]J. Heyd and G. E. Scuseria, J. Chem. Phys. **121**, 1187 (2004).

[45]J. P. Perdew and A. Zunger, Phys. Rev. B **23**, 5048 (1981).

[46]T. M. Henderson, J. Paier, and G. E. Scuseria, Phys. Status Solidi B **248**, 767 (2011).

[47]Q. Yan, P. Rinke, M. Scheffler, and C. G. Van de Walle, Appl. Phys. Lett. **95**, 121111 (2009).

[48]A. Zoroddu, F. Bernardini, P. Ruggerone, and V. Fiorentini, Phys. Rev. B **64**, 045208 (2001).

[49]V. Fiorentini and D. Vanderbilt (private communication).

[50]S. Muensit, E. M. Goldys, and I. L. Guy, Appl. Phys. Lett. **75**, 3965 (1999).

[51]F. Bernardini and V. Fiorentini, Appl. Phys. Lett. **80**, 4145 (2002).

[52]I. Vurgaftman and J. R. Meyer, J. Appl. Phys. **94**, 3675 (2003).

[53]S. Schulz, A. Berube, and E. P. O'Reilly, Phys. Rev. B **79**, 081401(R) (2009).

[54]S. Schulz, M. A. Caro, E. P. O'Reilly, and O. Marquardt, Phys. Status Solidi B **249**, 521 (2012).

[55]K. Shimada, Jpn. J. Appl. Phys. **45**, L358 (2006).

[56]S.-H. Wei, L. G. Ferreira, J. E. Bernard, and A. Zunger, Phys. Rev. B **42**, 9622 (1990).

[57]F. Bernardini and V. Fiorentini, Phys. Status Solidi A **190**, 65 (2002).

[58]G. Bester and A. Zunger, Phys. Rev. B **71**, 045318 (2005).

[59]J. D. Jackson, *Classical Electrodynamics*, 3rd ed. (Wiley, New York, 1999).

[60]Nonpolar QWs structures have precisely been proposed as a possible solution to the built-in field issue in nitride heterostructures, see T. Paskova, Phys. Status Solidi B **245**, 1011 (2008).

[61]P. N. Keating, Phys. Rev. **145**, 637 (1966).

[62]C. Pryor, J. Kim, L. W. Wang, A. J. Williamson, and A. Zunger, J. Appl. Phys. **83**, 2546 (1998).

[63]D. Camacho and Y. M. Niquet, Physica E **42**, 1361 (2010).

[64]R. M. Martin, Phys. Rev. B **6**, 4546 (1972).

[65]P. G. Moses, M. Miao, Q. Yan, and C. G. Van de Walle, J. Chem. Phys. **134**, 084703 (2011).

[66]J. A. Chan, J. Z. Liu, and A. Zunger, Phys. Rev. B **82**, 045112 (2010).

[67]E. P. O'Reilly, A. Lindsay, P. J. Klar, A. Polimeni, and M. Capizzi, Semicond. Sci. Technol. **24**, 033001 (2009).

[68]S. Schulz, S. Schumacher, and G. Czycholl, Eur. Phys. J. B **64**, 51 (2008).

[69]Q. Yan, P. Rinke, M. Scheffler, and C. G. Van de Walle, Appl. Phys. Lett. **97**, 181102 (2010).

[70]A. Kobayashi, O. F. Sankey, S. M. Volz, and J. D. Dow, Phys. Rev. B **28**, 935 (1983).

[71]M. Murayama and T. Nakayama, Phys. Rev. B **49**, 4710 (1994).

[72]K. Leung, S. Pokrant, and K. B. Whaley, Phys. Rev. B **57**, 12291 (1998).
[73]M. A. Caro, S. Schulz, and E. P. O'Reilly, Phys. Rev. B **86**, 099901(E) (2012).
[74]P. Vogl, H. P. Hjalmarson, and J. D. Dow, J. Phys. Chem. Solids **44**, 365 (1983).
[75]E. P. O'Reilly, A. Lindsay, S. Tomić, and M. Kamal-Saadi, Semicond. Sci. Technol. **17**, 870 (2002).
[76]Z. Q. Li and W. Pötz, Phys. Rev. B **46**, 2109 (1992).
[77]T. B. Boykin, N. Kharche, G. Klimeck, and M. Korkusinski, J. Phys.: Condens. Matter **19**, 036203 (2007).
[78]J.-M. Jancu, R. Scholz, F. Beltram, and F. Bassani, Phys. Rev. B **57**, 6493 (1998).
[79]T. B. Boykin, G. Klimeck, R. C. Bowen, and F. Oyafuso, Phys. Rev. B **66**, 125207 (2002).
[80]M. Winkelnkemper, A. Schliwa, and D. Bimberg, Phys. Rev. B **74**, 155322 (2006).
[81]S. Schulz, T. J. Badcock, M. A. Moram, P. Dawson, M. J. Kappers, C. J. Humphreys, and E. P. O'Reilly, Phys. Rev. B **82**, 125318 (2010).
[82]Note that the quantities a_2 and a_1 given by Vurgaftman and Meyer in their 2003 review article[52] *are not* the CB deformation potentials a_{cp} and a_{ct}, respectively. The quantities denoted by a_1 and a_2 in Ref. 52 are the *band-gap* deformation potentials, e.g., $a_1 = a_{cp} - D_1$ and $a_2 = a_{ct} - D_2$.
[83]Note that the definition of the strain matrix done by Pryor *et al.*[62] is related to ours via a transposition operation.
[84]V. Ranjan, L. Bellaiche, and E. J. Walter, Phys. Rev. Lett. **90**, 257602 (2003).
[85]T. Saito and Y. Arakawa, Physica E **15**, 169 (2002).
[86]K. Schuh, S. Barthel, O. Marquardt, T. Hickel, J. Neugebauer, G. Czycholl, and F. Jahnke, Appl. Phys. Lett. **100**, 092103 (2012).
[87]M. J. Galtrey, R. A. Oliver, M. J. Kappers, C. J. Humphreys, D. J. Stokes, P. H. Clifton, and A. Cerezo, Appl. Phys. Lett. **90**, 061903 (2007).
[88]C. J. Humphreys, Philos. Mag. **87**, 1971 (2007).
[89]M. D. McCluskey, C. G. Van de Walle, L. T. Romano, B. S. Krusor, and N. M. Johnson, J. Appl. Phys. **93**, 4340 (2003).
[90]P. Schley, R. Goldhahn, A. T. Winzer, G. Gobsch, V. Cimalla, O. Ambacher, H. Lu, W. J. Schaff, M. Kurouchi, Y. Nanishi, M. Rakel, C. Cobet, and N. Esser, Phys. Rev. B **75**, 205204 (2007).
[91]E. Sakalauskas, Ö. Tuna, A. Kraus, H. Bremers, U. Rossow, C. Giesen, M. Heuken, A. Hangleiter, G. Gobsch, and R. Goldhahn, Phys. Status Solidi B **249**, 485 (2012).
[92]S. Schulz, M. A. Caro, L.-T. Tan, P. J. Parbrook, R. W. Martin, and E. P. O'Reilly, Appl. Phys. Express **6**, 121001 (2013).
[93]C. Wetzel, T. Takeuchi, S. Yamaguchi, H. Katoh, H. Amano, and I. Akasaki, Appl. Phys. Lett. **73**, 1994 (1998).
[94]M. D. McCluskey, C. G. V. de Walle, C. P. Master, L. T. Romano, and N. M. Johnson, Appl. Phys. Lett. **72**, 2725 (1998).
[95]I. Gorczyca, S. P. Łepkowski, T. Suski, N. E. Christensen, and A. Svane, Phys. Rev. B **80**, 075202 (2009).
[96]P. Rinke, M. Winkelnkemper, A. Qteish, D. Bimberg, J. Neugebauer, and M. Scheffler, Phys. Rev. B **77**, 075202 (2008).
[97]S. Schulz and E. P. O'Reilly, Phys. Status Solidi B **249**, 516 (2012).
[98]J. Simon, N. T. Pelekanos, C. Adelmann, E. Martinez-Guerrero, R. André, B. Daudin, L. S. Dang, and H. Mariette, Phys. Rev. B **68**, 035312 (2003).
[99]R. G. Barrera, O. Guzman, and B. Balaguer, Am. J. Phys. **46**, 11 (1978).
[100]The strain field will not vanish in the barrier material immediately around a QD but will effectively be zero far away from it, see, for instance, Ref. 62.